An Unconditionally Energy-Stable Scheme for the Convective Heat Transfer Equation

Abstract

Purpose-This paper aims to present an unconditionally energy stable scheme for approximating the convective heat transfer equation.

Design/Methodology/Approach - The scheme stems from the generalized Positive Auxiliary Variable (gPAV) idea and exploits a special treatment for the convection term. The original convection term is replaced by its linear approximation plus a correction term, which is under the control of an auxiliary variable. The scheme entails the computation of two temperature fields within each time step, and the linear algebraic system resulting from the discretization involves a coefficient matrix that is updated periodically. This auxiliary variable is given by a well-defined explicit formula that guarantees the positivity of its computed value.

Findings - Compared with the semi-implicit scheme and the gPAV-based scheme without the treatment on the convection term, the current scheme can provide an expanded accuracy range and achieve more accurate simulations at large (or fairly large) time step sizes. Extensive numerical experiments have been presented to demonstrate the accuracy and stability performance of the scheme developed herein.

Originality/value - This study shows the unconditional discrete energy stability property of the current scheme, irrespective of the time step sizes.

Keywords Energy stability, Generalized positive auxiliary variable, Heat transfer, Navier-Stokes equations, Unconditional stability, Auxiliary variable.

1. Introduction

In this paper, we consider the numerical approximations of the convective heat transfer equation, which in combination with the incompressible Navier-Stokes equations constitutes a vital basis for heat transfer and fluid dynamics (Bo et al. (1995); Yan et al. (2022); Liu et al. (2020)). Convective heat transfer problems are common in nature and have been applied in a wide range of engineering and science fields, such as energy systems, material production, solar energy, and electronic cooling. The development of efficient numerical algorithms for the equation can have implications in the field of convective heat transfer and beyond.

This work focus on proposing an unconditional energy-stable scheme for the convective heat transfer problems. Energy stability is an attractive property in the numerical approximation and simulation of partial differential equations described in dissipative systems. An energy-stable approximation means that the system can maintain the energy dissipative (conservative) nature on the discrete level, which is not only consistent with important aspects of the underlying structure of continuous systems, but also provides a numerical stability control in practical computer simulations, allowing large time steps to be applied to computer simulations. Therefore, for the simulation of dissipative systems including but not limited to the Navier-Stokes (Lin et al. (2020a,b)), Cahn-Hilliard (Yang et al. (2019); Qian et al. (2020)) and convective heat transfer equations (Zhang & Yang (2020); Chandra & Chhabra (2011)), energy stability is a highly desirable property for the numerical algorithm of the systems.

The main challenge encountered in the numerical solution of the convective heat transfer equation arises from the coupling of the temperature and velocity fields, represented by the convective term. The most commonly used method is semi-implicit type schemes, which typically treat the convection term explicitly and thus can provide a natural and favorable way to decouple the temperature and velocity fields. Within a time step, the semi-implicit scheme only requires solving linear algebraic systems with a constant and time-independent coefficient matrix that can be pre-computed. Thanks to the low computational cost, the semi-implicit type schemes have been widely used in the simulations of convective heat transfer in fluid flow (Woodruff (2022); Bhinder et al. (2012); Chandra & Chhabra (2011); Wang & Pepper (2009); Feldman (2018); Soo et al. (2017); Liu et al. (2020)). A downside of the schemes is their conditional stability. Stable computation can be achieved only when the time step is small enough. However, the practitioners of computational heat transfer always desire to use larger time step sizes in computer simulations.

Energy-stable type schemes present a favorable method to alleviate the time step size constraint encountered with semi-implicit schemes. The attractive property of the energy stable schemes lies in the preservation of the energy dissipation on the discrete level, which can provide a control on the numerical stability. The potential drawback of energy-stable schemes is their computational cost. Because these schemes oftentimes entail the solution of a nonlinear algebraic system or a linear algebraic system multiple times, their computational cost per time step is typically higher than the semi-implicit type schemes, we refer to Celledoni et al. (2012); Shen et al. (2018); Yang (2016); Dahlby & Owren (2011); Eidnes et al. (2018) for example. The focus of the current work is to develop an unconditional energy-stable scheme with a relatively low computational cost for the convective heat transfer equation.

A number of energy stable schemes have been proposed and applied in the approximation of incompressible Navier-Stokes equations (Chen et al. (2018); Jiang et al. (2016); Labovsky et al. (2009); Simo & Armero (1994); Verstappen & Veldman (2003); Lin et al. (2019, 2020a); Sanderse (2013)). These schemes can effectively alleviate the time step size constraints faced by semi-implicit schemes, which represents a major precondition for simulating the convective heat transfer problems efficiently. In the past few years, the use of auxiliary variables turns out to be particularly effective in devising energy-stable schemes. Two prominent examples of such methods are the scalar auxiliary variable (SAV) Shen et al. (2018) and the invariant energy quadratization (IEQ) Yang (2016); see e.g. (Cheng & Shen (2018); Gong et al. (2018); Li et al. (2019); Yang et al. (2019); Zhao et al. (2018)). These two kinds of schemes have been employed in the approximation of the dendritic solidification systems (Zhang & Yang (2020); Chen & Yang (2019)), which involve the convective heat transfer equation. In both IEQ and SAV, the discrete energy stability of their resultant numerical schemes is built on the use of the auxiliary variable/field in the form of square root functions. An interesting recent development in this area is Yang & Dong (2020), which describes a systematic roadmap for devising discretely energy-stable schemes for general dissipative systems. This roadmap is developed based on the generalized Positive Auxiliary Variable (gPAV) method, which employs a scalar-valued number as the auxiliary variable and endows the discrete energy stability to the resultant scheme. Compared to the related works in (Shen et al. (2018); Yang & Dong (2019); Yang (2016)), the gPAV method can allow using a general class of function form to define the auxiliary variable, and ensure the positivity of the computed values of the generalized auxiliary variable. Several works (Lin et al. (2020a,b); Qian et al. (2020)) have employed the roadmap to devise the

energy-stable scheme, which turn out that the gPAV method is particular effective to achieve the discrete energy stability for general dissipative partial differential equations. Further development of this approach is discussed very recently in Lin et al. (2020b). This work proposes a numerical scheme for the incompressible Navier-Stokes equations under the gPAV framework and introduces a numerical treatment to the nonlinear term.

In the current work, we present an unconditionally energy stable scheme for the convective heat transfer equation. This scheme can achieve accurate simulations at large or fairly large time step sizes without seriously sacrificing the computational cost. The prominent feature of the scheme lies in a gPAV-based reformulation and a numerical treatment for the convection term inspired by Lin et al. (2020b). In the reformulated system, the convection term is replaced by its linear approximation plus a correction term. The correction term is then controlled by an auxiliary variable to guarantee unconditional energy stability.

The proposed algorithm requires computing two copies of the temperature field within a time step by solving a linear algebraic system that is with a periodically updated coefficient matrix. The updating frequency of the coefficient matrix can be specified by the user. The auxiliary variable is computed by a well-defined explicit formulation that guarantees the positivity of its computed values, which is consistent with the physical definition. The unconditional stability of the scheme has been shown. The reported results demonstrated that the simulation with the proposed algorithm can achieve accurate results at large or fairly large time step sizes, depending on the Reynolds number. It is observed that employing the gPAV method directly will lead to a higher computational cost compared to the semi-implicit scheme, which is an undesirable aspect of the new scheme. By introducing a numerical treatment on the convection term, our scheme substantially expands the accuracy range for the time step size and thus makes the proposed scheme favorable for simulating convective heat transfer problems efficiently.

The contribution of this work lies in the unconditional energy-stable scheme for the convective heat transfer system developed herein. This specifically includes: (i) the introduction of the gPAV approach into the resultant reformulation of the convective heat transfer system, (ii) the numerical scheme for approximating the reformulated system of equations, (iii) an improved accuracy under a relatively low computational cost.

The rest of the paper is structured as follows. In Section 2 we first derive the reformulation of the convective heat transfer equation utilizing the gPAV approach and present the energy stable

scheme for the reformulated system. The discretely energy stable property of the scheme is proved. We also present the solution algorithm of the scheme and its detailed implementation based on high-order spectral elements (Karniadakis & Sherwin (2005); Blackburn & Henderson (1999); Zheng & Dong (2011); Sherwin & Karniadakis (1995)). In Section 3 we demonstrate the convergence rates using a manufactured analytic solution and test the accuracy and performance of the proposed scheme using two canonical problems involving convective heat transfer in fluid flows. Section 4 concludes discussions with some closing remarks. Appendix A provides a summary of the numerical algorithm for the incompressible Navier-Stokes equations, which are employed in the current work. Appendix B provides the commonly used semi-implicit algorithms for solving the convective heat transfer equation. In addition, derivations of two equations in the main text are given in Appendix C.

2. Discretely energy-stable scheme for the convective heat transfer equation

2.1. Convective heat transfer equation and energy balance relation

Consider a domain Ω (with boundary $\partial\Omega$) in two or three dimensions, and an incompressible flow contained in the domain. The convective heat transfer problem is then described by the following system of equations in non-dimensional form:

$$\frac{\partial \mathbf{u}}{\partial t} + \mathbf{u}\cdot\nabla\mathbf{u} + \nabla p - \nu\nabla^2\mathbf{u} = \mathbf{f}(\mathbf{x},t), \tag{1a}$$

$$\nabla\cdot\mathbf{u} = 0, \tag{1b}$$

$$\frac{\partial T}{\partial t} + \mathbf{u}\cdot\nabla T = \alpha\nabla^2 T + g(\mathbf{x},t), \tag{1c}$$

where $\mathbf{u}(\mathbf{x},t)$ and $p(\mathbf{x},t)$ are respectively the non-dimensional velocity and pressure, $\mathbf{f}(\mathbf{x},t)$ is an external body force, $T(\mathbf{x},t)$ is the non-dimensional temperature, $g(\mathbf{x},t)$ is an external volumetric heat source term, and $\mathbf{x}$ and t are the spatial coordinate and time. ν is non-dimensional viscosity or the reciprocal of the Reynolds number Re,

$$\nu = \frac{1}{Re} = \frac{\nu_f}{U_0 L}, \tag{2}$$

where ν_f is the kinematic viscosity of the fluid, and U_0 and L are the velocity and length scales. α denotes the non-dimensional thermal diffusivity or the reciprocal of the Peclet number,

$$\alpha = \frac{1}{P_e} = \frac{\alpha_f}{U_0 L}, \tag{3}$$

where α_f is the thermal diffusivity of the fluid. In the current work, we assume that both ν and α are constant, and no viscous dissipation of energy. Only one-way coupling will be considered between the flow and the temperature, i.e., the flow affects the temperature distribution while the effect of the temperature on the fluid flow will be ignored. Note that Eqs. (1a)-(1b) for describing the motion of the flow are the incompressible Navier-Stokes equations.

On the domain boundary $\partial\Omega$, we assume that the velocity is known,

$$\mathbf{u} = \mathbf{w}(\mathbf{x}, t), \quad \text{on } \partial\Omega, \tag{4}$$

where $\mathbf{w}$ denotes the boundary velocity. In order to provide a uniquely defined pressure, we impose the often-used condition in the current work,

$$\int_\Omega p d\Omega = 0 \tag{5}$$

In terms of temperature, we assume that $\partial\Omega$ consists of two non-overlapping types: $\partial\Omega = \partial\Omega_d \cup \partial\Omega_n$. We impose the Dirichlet boundary condition on $\partial\Omega_d$,

$$T = T_d(\mathbf{x}, t), \quad \text{on } \partial\Omega_d, \tag{6}$$

where T_d is the known boundary temperature, and the Neumann boundary condition on $\partial\Omega_n$,

$$\mathbf{n} \cdot \nabla T = g_c(\mathbf{x}, t), \quad \text{on } \partial\Omega_n, \tag{7}$$

where $g_c(\mathbf{x}, t)$ is a prescribed term associated with the heat flux on boundary and $\mathbf{n}$ is the outward-pointing unit vector normal to the boundary $\partial\Omega_n$. In addition, the system is supplemented by the initial conditions for the velocity,

$$\mathbf{u}(\mathbf{x}, 0) = \mathbf{u}_{in}(\mathbf{x}), \tag{8}$$

and for the temperature,

$$T(\mathbf{x}, 0) = T_{in}(\mathbf{x}), \tag{9}$$

where $\mathbf{u}_{in}$ and T_{in} denote the initial velocity and temperature distribution.

We focus on the numerical approximation of the convective heat transfer equation (1c). Multiplying (1c) by T and integrating over $\partial\Omega$, we obtain an energy balance equation as follows,

$$\begin{aligned}\frac{\partial}{\partial t}\int_\Omega \frac{1}{2}|T|^2 d\Omega = -\alpha\int_\Omega |\nabla T|^2 d\Omega + \int_\Omega g(\mathbf{x},t)T d\Omega \\ + \int_{\partial\Omega}\left[\alpha\mathbf{n}\cdot\nabla T - \frac{1}{2}(\mathbf{n}\cdot\mathbf{u})T\right]T dA,\end{aligned} \tag{10}$$

where integration by parts and the divergence theorem are used. With the boundary conditions (6) and (7), the energy balance equation (10) is then transformed into

$$\begin{aligned}&\frac{\partial}{\partial t}\int_\Omega \frac{1}{2}|T|^2 d\Omega = -\alpha\int_\Omega |\nabla T|^2 d\Omega + \int_\Omega g(\mathbf{x},t)T d\Omega \\ &+ \int_{\partial\Omega_d}\left[\alpha\mathbf{n}\cdot\nabla T - \frac{1}{2}(\mathbf{n}\cdot\mathbf{u})T_d\right]T_d dA + \int_{\partial\Omega_n}\left[\alpha g_c(\mathbf{x},t) - \frac{1}{2}(\mathbf{n}\cdot\mathbf{u})T\right]T dA.\end{aligned} \tag{11}$$

2.2. gPAV-reformulated system

In order to facilitate the development of the discretely energy-stable scheme, we will firstly reformulate the system consisting of Eq. (1c), the boundary conditions (6) and (7) and the initial condition (9) into an equivalent form.

Define a shifted energy,

$$E(t) = E(T) = \int_\Omega \frac{1}{2}|T|^2 d\Omega + C_0, \tag{12}$$

where C_0 is a chosen energy constant such that $E(t) > 0$ for all $t \geq 0$. For a convective heat transfer system, the energy is bounded from below, thus can always be found and be considered as the lower bound of the system energy. Based on the gPAV framework Yang & Dong (2020), we introduce an auxiliary variable $R(t)$ based on $E(t)$,

$$E(t) = R(t)^2, \tag{13a}$$

$$R(t) = \sqrt{E(t)}. \tag{13b}$$

Then $R(t)$ satisfies the following dynamic equation,

$$2R\frac{dR}{dt} = \int_\Omega T \cdot \frac{\partial T}{\partial t} d\Omega. \tag{14}$$

Note that both $R(t)$ and $E(t)$ are scalar numbers instead of field variables, and so $\frac{R^2(t)}{E(t)} = 1$.

With the variables defined above, we rewrite the Eq. (1c) into the following equivalent form,

$$\frac{\partial T}{\partial t} + M(\mathbf{u_0}, T) - \alpha\nabla^2 T = \frac{R^2(t)}{E(t)}[M(\mathbf{u_0}, T) - N(\mathbf{u}, T)] + g(\mathbf{x}, t), \tag{15}$$

where $N(\mathbf{u}, T) = \mathbf{u} \cdot \nabla T$, and $M(\mathbf{u_0}, T)$ is a linear approximation of $N(\mathbf{u}, T)$ defined as following,

$$M(\mathbf{u_0}, T) = \mathbf{u}_0 \cdot \nabla T + \frac{1}{2}(\nabla \cdot \mathbf{u}_0)\, T, \tag{16}$$

where $\mathbf{u_0}$ is a chosen velocity that can be updated occasionally in time. In the presented work, we set $\mathbf{u_0}$ to be the velocity field at every k_0-th time step, where k_0 is an integer parameter provided by the user. It means that the velocity field is updated only once at every k_0 time step.

Following the gPAV idea in Yang & Dong (2020) and also the work Lin et al. (2020b), we incorporate a number of zero term into the right hand side (RHS) of Eq. (14) and rewrite the

equation as follows,

$$
\begin{aligned}
2R\frac{dR}{dt} &= \int_\Omega T\cdot\frac{\partial T}{\partial t}d\Omega + \left[\frac{R^2(t)}{E(t)}-1\right]\int_\Omega \left[-M(\mathbf{u_0},T)+\alpha\nabla^2 T+g(\mathbf{x},t)\right]Td\Omega \\
&+ \frac{R^2(t)}{E(t)}\left(\int_\Omega \left[M(\mathbf{u_0},T)-N(\mathbf{u},T)\right]Td\Omega - \int_\Omega \left[M(\mathbf{u_0},T)-N(\mathbf{u},T)\right]Td\Omega\right) \\
&+ \left[1-\frac{R^2(t)}{E(t)}\right]\left(\left|\int_\Omega g(\mathbf{x},t)Td\Omega\right| + \left|\int_{\partial\Omega}\left[\alpha\mathbf{n}\cdot\nabla T-\frac{1}{2}(\mathbf{n}\cdot\mathbf{u})T\right]TdA\right|\right) \\
&= \int_\Omega T\cdot\frac{\partial T}{\partial t}d\Omega + \frac{R^2(t)}{E(t)}\int_\Omega \left[-N(\mathbf{u},T)+\alpha\nabla^2 T+g(\mathbf{x},t)\right]Td\Omega \\
&- \int_\Omega\left[-M(\mathbf{u_0},T)+\alpha\nabla^2 T+g(\mathbf{x},t)+\frac{R^2(t)}{E(t)}\left(M(\mathbf{u_0},T)-N(\mathbf{u},T)\right)\right]Td\Omega \\
&+ \left[1-\frac{R^2(t)}{E(t)}\right]\left(\left|\int_\Omega g(\mathbf{x},t)Td\Omega\right| + \left|\int_{\partial\Omega_d}\left[\alpha\mathbf{n}\cdot\nabla T-\frac{1}{2}(\mathbf{n}\cdot\mathbf{u})T_d\right]T_d dA\right.\right. \\
&\left.\left.+\int_{\partial\Omega_n}\left[\alpha g_c(\mathbf{x},t)-\frac{1}{2}(\mathbf{n}\cdot\mathbf{u})T\right]TdA\right|\right).
\end{aligned}
\tag{17}
$$

In the above equation, $|(\cdot)|$ denotes the absolute value of $(\cdot)$. In light of Eq. (11), we further transform the Eq. (17) into the final reformulated equivalent form

$$
\begin{aligned}
2R\frac{dR}{dt} &= \int_\Omega T\cdot\frac{\partial T}{\partial t}d\Omega \\
&+ \frac{R^2(t)}{E(t)}\left[-\alpha\int_\Omega|\nabla T|^2 d\Omega+\int_\Omega g(\mathbf{x},t)Td\Omega\right. \\
&\left.+\int_{\partial\Omega_d}\left[\alpha\mathbf{n}\cdot\nabla T-\frac{1}{2}(\mathbf{n}\cdot\mathbf{u})T_d\right]T_d dA+\int_{\partial\Omega_n}\left[\alpha g_c(\mathbf{x},t)-\frac{1}{2}(\mathbf{n}\cdot\mathbf{u})T\right]TdA\right] \\
&- \int_\Omega\left[-M(\mathbf{u_0},T)+\alpha\nabla^2 T+g(\mathbf{x},t)+\frac{R^2(t)}{E(t)}(M(\mathbf{u_0},T)-N(\mathbf{u},T))\right]Td\Omega \\
&+ \left[1-\frac{R^2(t)}{E(t)}\right]\left(\left|\int_\Omega g(\mathbf{x},t)Td\Omega\right| + \left|\int_{\partial\Omega_d}\left[\alpha\mathbf{n}\cdot\nabla T-\frac{1}{2}(\mathbf{n}\cdot\mathbf{u})T_d\right]T_d dA\right.\right. \\
&\left.\left.+\int_{\partial\Omega_n}\left[\alpha g_c(\mathbf{x},t)-\frac{1}{2}(\mathbf{n}\cdot\mathbf{u})T\right]TdA\right|\right).
\end{aligned}
\tag{18}
$$

The reformulated system consists of Eqs. (15) and (58), the boundary conditions Eqs. (6) and

(7), and the initial condition Eq. (9) for temperature and the following initial condition for $R(t)$,

$$R(0) = \sqrt{E(0)}, \text{ where } E(0) = \int_\Omega \frac{1}{2} |T_{in}|^2 \, d\Omega + C_0. \tag{19}$$

In this system, the dynamic variables are $T(\mathbf{x}, t)$ and $R(t)$, which are coupled with Eqs. (15) and (58). $E(t)$ is given by Eq. (12). Note that $R(t)$ is obtained by solving the coupled system of equations, not by using Eq. (13b). So to this extent, $R(t)^2$ is an approximation of $E(t)$.

Remark 2.1. *It is worth noting that by modifying the original equation (1c) to equation (15), we put the convection term under the control of the auxiliary variable and introduce a special treatment for the convection term which helps to expand the accuracy range in the numerical simulations. The reformulated equation (15) is the equivalent form of equation (1c) on the continuous level. Based on the modification, the auxiliary variable is further given by a well-defined explicit formula that guarantees the positivity of its computed value. This also leads to an approximation of R that does not necessarily fulfill the relation $R^2 = E$ at the numerical level. Both the modification for convective heat transfer (including the boundary conditions) and the explicit formula of the auxiliary variable make up the reformulated system. In the reformulated system, the two dynamic variables are T and R, which are obtained by solving the coupled system of equations (15) and (58) when performing numerical approximation. So to this extent, R^2 is an approximation of E. With the gPAV style reformulation and the proper scheme design, the unconditional energy stability of the system can be guaranteed, which will be proven in the next section.*

2.3. Numerical scheme and unconditional energy stability

We next present the unconditional energy-stable scheme for the reformulated heat transfer system consisting of Eqs. (15) and (58), the boundary conditions Eqs. (6) and (7), as well as the initial conditions Eq. (9) and (19). We assume that the velocity $\mathbf{u}$ has already been calculated by solving the incompressible Navier-Stokes equations (1a) and (1b), together with the boundary condition (4) and (5).

Let $n \geq 0$ denote the time step index, and $(\cdot)^n$ denotes $(\cdot)$ at time step n. Define

$$T^0 = T_{in}, \quad R^0 = R(0). \tag{20}$$

Then given (T^n, R^n) and these values at previous time steps, we compute the T^{n+1} through the following scheme:

For T^{n+1}:

$$\begin{aligned}&\frac{\gamma_0 T^{n+1}-\hat{T}}{\Delta t}+M(\mathbf{u_0},T^{n+1})-\alpha\nabla^2 T^{n+1}\\&=\xi\left[M(\mathbf{u_0},T^{*,n+1})-N(\mathbf{u}^{n+1},T^{*,n+1})\right]+g^{n+1}(\mathbf{x},t),\end{aligned}\tag{21a}$$

$$T^{n+1}=T_d^{n+1}(\mathbf{x},t),\qquad \text{on } \partial\Omega_d,\tag{21b}$$

$$\mathbf{n}\cdot\nabla T^{n+1}=g_c^{n+1}(\mathbf{x},t),\qquad \text{on } \partial\Omega_n,\tag{21c}$$

$$\xi=\frac{(R^{n+3/2})^2}{E(\overline{T}^{n+3/2})},\tag{21d}$$

$$E(\overline{T}^{n+3/2})=\int_\Omega \frac{1}{2}\left|\overline{T}^{n+3/2}\right|^2 d\Omega+C_0.\tag{21e}$$

For R^{n+1}:

$$\begin{aligned}&\left(\frac{3}{2}R^{n+1}+R^n-\frac{1}{2}R^{n-1}\right)\frac{\frac{3}{2}R^{n+1}-2R^n+\frac{1}{2}R^{n-1}}{\Delta t}\\&=\int_\Omega\frac{\gamma_0 T^{n+1}-\hat{T}}{\Delta t}T^{n+1}d\Omega\\&-\int_\Omega\left[-M(\mathbf{u_0},T^{n+1})+\alpha\nabla^2T^{n+1}+g^{n+1}+\xi(M(\mathbf{u_0},T^{*,n+1})-N(\mathbf{u^{n+1}},T^{*,n+1})\right]T^{n+1}d\Omega\\&+\xi\left(-\alpha\int_\Omega|\nabla\overline{T}^{n+1}|^2d\Omega+\int_\Omega g^{n+1}\overline{T}^{n+1}d\Omega+\int_{\partial\Omega_d}\left[\alpha\mathbf{n}\cdot\nabla\overline{T}^{n+1}-\frac{1}{2}(\mathbf{n}\cdot\mathbf{u}^{n+1})T_d^{n+1}\right]T_d^{n+1}dA\right.\\&\left.+\int_{\partial\Omega_n}\left[\alpha g_c^{n+1}-\frac{1}{2}(\mathbf{n}\cdot\mathbf{u}^{n+1})\overline{T}^{n+1}\right]\overline{T}^{n+1}dA\right)\\&+(1-\xi)\left(\left|\int_\Omega g^{n+1}(\mathbf{x},t)\overline{T}^{n+1}d\Omega\right|+\left|\int_{\partial\Omega_d}\left[\alpha\mathbf{n}\cdot\nabla\overline{T}^{n+1}-\frac{1}{2}(\mathbf{n}\cdot\mathbf{u})T_d^{n+1}\right]T_d^{n+1}dA\right.\right.\\&\left.\left.+\int_{\partial\Omega_n}\left[\alpha g_c^{n+1}-\frac{1}{2}(\mathbf{n}\cdot\mathbf{u}^{n+1})\overline{T}^{n+1}\right]\overline{T}^{n+1}dA\right|\right),\end{aligned}\tag{22}$$

where Δt is the time step size. Let J ($J=1$ or 2) denote the temporal order of accuracy. $\frac{\gamma_0 T^{n+1}-\hat{T}}{\Delta t}$ is the approximation of $\frac{\partial T}{\partial t}\big|^{n+1}$ based on the J-th order backward differentiation formula (BDF), in

which

$$\gamma_0 = \begin{cases} 1, & J=1, \\ 3/2, & J=2; \end{cases} \quad \hat{T} = \begin{cases} T^n, & J=1, \\ 2T^n - \frac{1}{2}T^{n-1}, & J=2. \end{cases} \tag{23}$$

$T^{*,n+1}$ is a J-th order explicit approximation of T^{n+1}, given by

$$T^{*,n+1} = \begin{cases} T^n, & J=1, \\ 2T^n - T^{n-1}, & J=2. \end{cases} \tag{24}$$

$\overline{T}^{n+1}$ and $\overline{T}^{n+3/2}$ are second-order approximation of T^{n+1} and $T^{n+3/2}$ and will be given later. $R^{n+3/2}$ and $R^{n+1/2}$ are defined by

$$R^{n+3/2} = \frac{3}{2}R^{n+1} - \frac{1}{2}R^n, \quad R^{n+1/2} = \frac{3}{2}R^n - \frac{1}{2}R^{n-1}. \tag{25}$$

Besides, when dealing with the Eq. (22), we use the following relationship

$$\begin{aligned} &\left(\tfrac{3}{2}R^{n+1} + R^n - \tfrac{1}{2}R^{n-1}\right)\left(\tfrac{3}{2}R^{n+1} - 2R^n + \tfrac{1}{2}R^{n-1}\right) \\ &= \left(R^{n+3/2} + R^{n+1/2}\right)\left(R^{n+3/2} - R^{n+1/2}\right) = \left(R^{n+3/2}\right)^2 - \left(R^{n+1/2}\right)^2. \end{aligned} \tag{26}$$

The scheme presented by Eqs. (21a)-(22) is energy stable due to the following property.

Theorem 2.1. *In the absence of the external volumetric and boundary heat source terms (i.e. $g = 0$ and $g_c = 0$), and together with the velocity $\mathbf{w} = \mathbf{0}$ on $\partial\Omega$ and the temperature Dirichlet boundary $T_d = 0$ on $\partial\Omega_d$, the scheme (21a)-(22) satisfies the following property:*

$$\left(R^{n+3/2}\right)^2 - \left(R^{n+1/2}\right)^2 = -\xi\Delta t\alpha \int_\Omega |\nabla\overline{T}^{n+1}|^2 d\Omega \leq 0, \tag{27}$$

where $R^{n+3/2}$ and $R^{n+1/2}$ are defined by Eq. (25).

Proof. Multiplying the equation (21a) by T^{n+1}, and adding the resultant equation to Eq. (22), we arrive at

$$\left(R^{n+3/2}\right)^2 - \left(R^{n+1/2}\right)^2 = -\xi\Delta t\alpha \int_\Omega |\nabla\overline{T}^{n+1}|^2 d\Omega - \xi S_0\Delta t + S_1\Delta t, \tag{28}$$

where

$$\begin{cases} S_0 = (|B| - B) + (|C| - C)\,, \\ S_1 = |B| + |C|\,, \\ B = \displaystyle\int_\Omega g^{n+1}(\mathbf{x},t)\overline{T}^{n+1} d\Omega, \\ C = \displaystyle\int_{\partial\Omega_d} \left[\alpha \mathbf{n}\cdot\nabla\overline{T}^{n+1} - \frac{1}{2}\left(\mathbf{n}\cdot\mathbf{w}^{n+1}\right) T_d^{n+1}\right] T_d^{n+1} dA \\ \quad + \displaystyle\int_{\partial\Omega_n} \left[\alpha g_c^{n+1}(\mathbf{x},t) - \frac{1}{2}\left(\mathbf{n}\cdot\mathbf{w}^{n+1}\right)\overline{T}^{n+1}\right]\overline{T}^{n+1} dA. \end{cases} \tag{29}$$

If $g = 0$, $g_c = 0$, $\mathbf{w} = \mathbf{0}$, $T_d = 0$, then $S_0 = 0$ and $S_1 = 0$. Therefore equation (28) leads to (27). In light of Eq. (21d) and (21e), it can be noted that $\xi \geq 0$. We conclude that the inequality in (27) holds. □

2.4. Solution algorithm and implementation with high-order spectral elements

Let us now consider how to implement the scheme represented by Eqs. (21a)-(22). Note that the variable $R(t)$, ξ and $E(T)$ are scalar-valued numbers, instead of field functions. In addition, ξ is computed depending on T. Taking advantage of the fact that ξ is a scalar number, we introduce two field functions (T_1^{n+1}, T_2^{n+1}) as solutions of the following equations:

For T_1^{n+1}:

$$\begin{aligned} &\frac{\gamma_0 T_1^{n+1}}{\Delta t} + \mathbf{u}_0\cdot\nabla T_1^{n+1} + \frac{1}{2}\left(\nabla\cdot\mathbf{u}_0\right) T_1^{n+1} - \alpha\nabla^2 T_1^{n+1}, \\ &= g^{n+1}(\mathbf{x},t) + \frac{\hat{T}}{\Delta t}, \end{aligned} \tag{30a}$$

$$T_1^{n+1} = T_d^{n+1}(\mathbf{x},t), \quad \text{on } \partial\Omega_d, \tag{30b}$$

$$\mathbf{n}\cdot\nabla T_1^{n+1} = g_c^{n+1}(\mathbf{x},t), \quad \text{on } \partial\Omega_n. \tag{30c}$$

For T_2^{n+1}:

$$\begin{aligned}&\frac{\gamma_0 T_2^{n+1}}{\Delta t}+\mathbf{u}_0\cdot\nabla T_2^{n+1}+\frac{1}{2}\left(\nabla\cdot\mathbf{u}_0\right)T_2^{n+1}-\alpha\nabla^2 T_2^{n+1}\\&=M(\mathbf{u_0},T^{*,n+1})-N(\mathbf{u^{n+1}},T^{*,n+1}),\end{aligned}\tag{31a}$$

$$T_2^{n+1}=0,\quad \text{on } \partial\Omega_d,\tag{31b}$$

$$\mathbf{n}\cdot\nabla T_2^{n+1}=0,\quad \text{on } \partial\Omega_n.\tag{31c}$$

Then it is straightforward to verify that the solution to Eqs. (21a), (21b) and (21c) is given by,

$$T^{n+1}=T_1^{n+1}+\xi T_2^{n+1},\tag{32}$$

where T_1^{n+1}, T_2^{n+1} are the solutions of equations (30a) and (31a), and ξ is to be determined later.

With T_1^{n+1} and T_2^{n+1}, we define

$$\overline{T}^{n+1}=T_1^{n+1}+T_2^{n+1},\quad \overline{T}^{n+3/2}=\frac{3}{2}\overline{T}^{n+1}-\frac{1}{2}T^n,\tag{33}$$

which are second-order approximation of T^{n+1} and $T^{n+3/2}$, respectively. By Eq. (21d), we have

$$(R^{n+3/2})^2=\xi(E^{n+3/2}).\tag{34}$$

Note that Eq. (22) can be transformed into equation (28). Inserting Eq. (34) into equation (28), we can obtain the solution for ξ,

$$\xi=\frac{\left(R^{n+1/2}\right)^2+S_1\Delta t}{E\left[\overline{T}^{n+3/2}\right]+\left(A+S_0\right)\Delta t},\tag{35}$$

where S_0 and S_1 are given in (29), and

$$A=\alpha\int_\Omega|\nabla\overline{T}^{n+1}|^2 d\Omega.\tag{36}$$

With ξ known, T^{n+1} can be computed by equation (32). Using equations (35) and (21e), R^{n+1}

is computed as follows,

$$\begin{cases} R^{n+3/2} = \sqrt{\xi E\left[\overline{T}^{n+3/2}\right]}, \\ R^{n+1} = \frac{2}{3}R^{n+3/2} + \frac{1}{3}R^{n}. \end{cases} \tag{37}$$

It should be noted that in the proposed algorithm, the original convection term is replaced by its linear approximation plus a correction term, and the correction term is put under the control of an auxiliary variable. In the discrete temperature equation (21), the temperature in the linearized approximation of the convection term is approximated implicitly while the temperature in the correction term is given by its second-order explicit approximation. The utilized time integration scheme is the second-order backward differentiation formula. For the R equation (22), we do not use this equation directly. This equation is further transformed into equation (35). Therefore, we first calculate the value of the scalar number and then calculate the value of R using equation (37).

The equations (30a) and (31a) require to be solved for the field T_1^{n+1} and T_2^{n+1}. Let us next consider how to implement the proposed energy-stable scheme. We employ C^0-continuous high-order spectral elements for spatial discretization. Let $\varphi(\mathbf{x})$ denote an arbitrary test function that vanishes on $\partial\Omega_d$, i.e. $\varphi|_{\partial\Omega_d} = 0$. Multiplying φ to Eqs. (30a) and (31a), and integrating over the domain Ω, we obtain the weak form about T_1^{n+1} and T_2^{n+1} as follow,

For T_1^{n+1}:

$$\begin{aligned} &\int_\Omega \nabla T_1^{n+1}\cdot\nabla\varphi d\Omega + \frac{\gamma_0}{\alpha\Delta t}\int_\Omega T_1^{n+1}\varphi d\Omega + \frac{1}{\alpha}\int_\Omega \mathbf{u}_0\cdot\nabla T_1^{n+1}\varphi d\Omega + \frac{1}{\alpha}\int_\Omega \frac{1}{2}(\nabla\cdot\mathbf{u}_0)T_1^{n+1}\varphi d\Omega \\ &= \frac{1}{\alpha}\int_\Omega\left(g^{n+1} + \frac{\hat{T}}{\Delta t}\right)\varphi d\Omega + \int_{\partial\Omega_n} g_c^{n+1}\varphi dA, \quad \forall\varphi \text{ with } \varphi|_{\partial\Omega_d} = 0. \end{aligned} \tag{38}$$

For T_2^{n+1}:

$$\begin{aligned} &\int_\Omega \nabla T_2^{n+1}\cdot\nabla\varphi d\Omega + \frac{\gamma_0}{\alpha\Delta t}\int_\Omega T_2^{n+1}\varphi d\Omega + \frac{1}{\alpha}\int_\Omega \mathbf{u}_0\cdot\nabla T_2^{n+1}\varphi d\Omega + \frac{1}{\alpha}\int_\Omega \frac{1}{2}(\nabla\cdot\mathbf{u}_0)T_2^{n+1}\varphi d\Omega \\ &= \frac{1}{\alpha}\int_\Omega\left(\mathbf{u}_0\cdot\nabla T^{*,n+1} + \frac{1}{2}\left(\nabla\cdot\mathbf{u}_0\right)T^{*,n+1} - \mathbf{u^{n+1}}\cdot\nabla T^{*,n+1}\right)\varphi d\Omega, \quad \forall\varphi \text{ with } \varphi|_{\partial\Omega_d} = 0. \end{aligned} \tag{39}$$

where we have used integration by part, the divergence theorem, and Eqs. (30c) and (31c). The weak form (38) and (39), together with the Dirichlet condition (30b) and (31b), can be discretized

using C^0 spectral elements in a standard way Karniadakis & Sherwin (2005). Note that the $\mathbf{u_0}$ is set to update every k_0 time steps when solving the temperature field.

Combining the above discussion, we arrive at the final solution algorithm within a time step:

(i) compute the velocity $\mathbf{u^{n+1}}$ and pressure p^{n+1} using the algorithm from the Appendix A.

(ii) solve equation (38) together with (30b) for the temperature T_1^{n+1}
solve equation (39) together with (31b) for the temperature T_2^{n+1}.

(iii) compute the coefficients A, S0, S1 based on (36) and (29);

(iv) compute ξ from equation (35)

(v) compute T^{n+1} from equation (32) and R^{n+1} from equation (37).

Figure 1 shows a flowchart of the proposed algorithm for solving the convective heat transfer equation. The unknown variables to be calculated and the related equations to be solved are both provided. All the equations involved therein are presented in their weak form, which can be directly solved using C^0- continuous high-order spectral elements method.

Remark 2.2. *Note that a modified scheme can be obtained by choosing* $M(\mathbf{u}) = 0$ *in Eq.(15) and it can be implemented using the same algorithm represented by Eqs.(21a)-(22). With this modified scheme the discrete energy stability as given by* **Theorem 2.1** still holds. *Compared to the current scheme, the strength of the modification is that upon discretization the temperature linear systems only involve constant coefficient matrix that can be pre-computed. However, the modified scheme is less accurate at moderate or fairly large time step size and its accurancy range is significantly influenced by the parameter* C_0. *These points will be demonstrated by numerical experiments in Section 3.*

Remark 2.3. *In the current work, the energy stable scheme requires the computation of two temperature fields within each time step by solving the temperature linear algebraic system involving a coefficient matrix updated periodically. The auxiliary variable is given by a well-defined explicit formulation. Thus, no Newton-type method is used when solving the heat transfer system. The coefficient matrix in the temperature linear algebraic systems is non-symmetric (but positive definite) and is solved using the bi-conjugate gradient stabilized (BiCGStab) linear solver. We use a simple Jacobi pre-conditioner for all the test problems presented subsequently.*

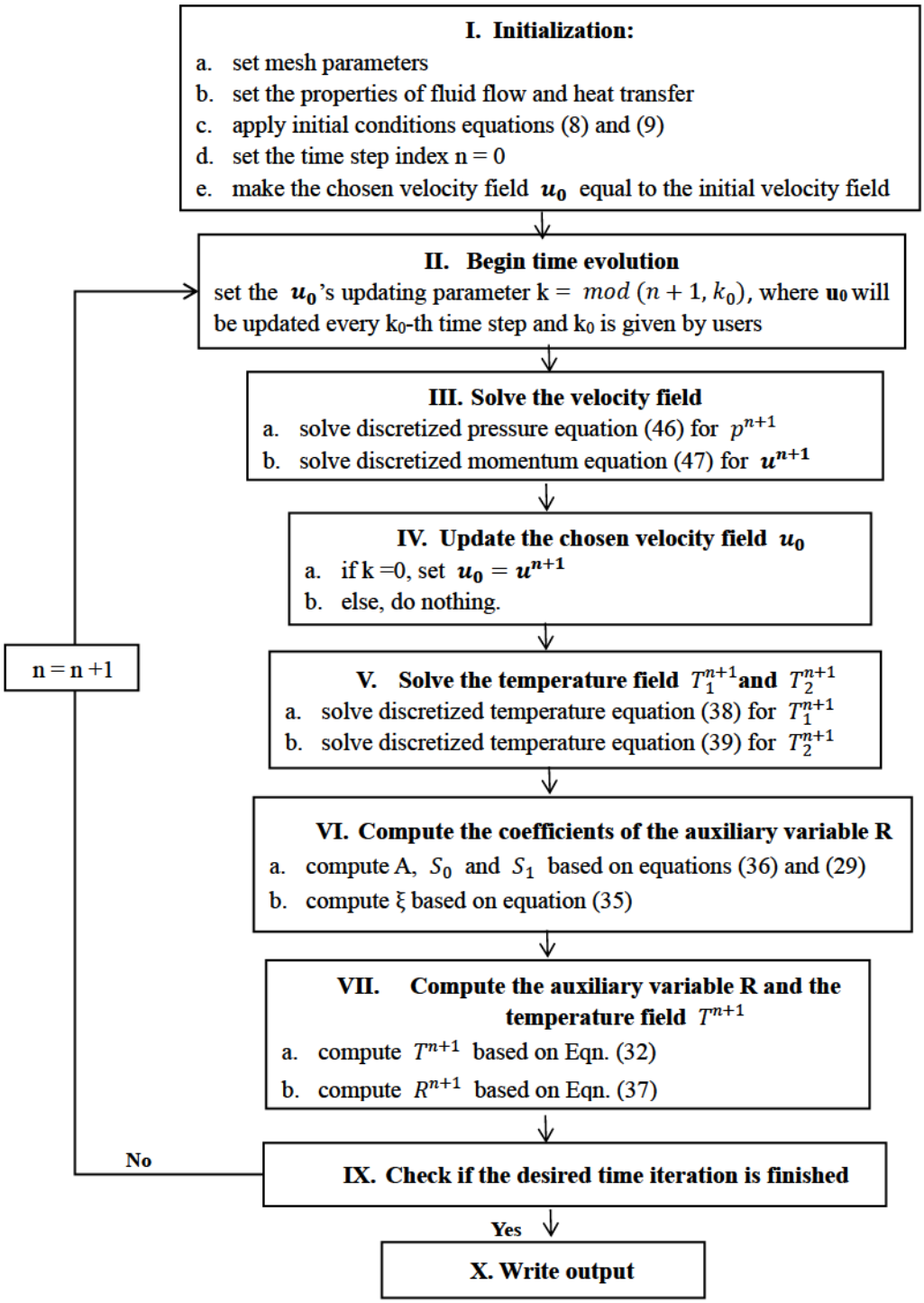

Figure 1 Flowchart of the proposed numerical algorithm for the convective heat transfer equation.

3. Representative simulations

In this section, we use several convective heat transfer problems in two dimensions to test the performance of the scheme presented above. The spatial and temporal convergence rates of the method are firstly demonstrated, and then the effects of the algorithmic parameters on the simulation results will be studied, especially the stability and the accuracy at large time step sizes will be demonstrated. A survey of literature indicates the semi-implicit schemes based on the second-order backward differentiation formula (BDF-2) and based on the Crank-Nicolson/Adams-Bashforth (CNAB-2) scheme are the most commonly-used methods for heat transfer problems; see e.g. Liu et al. (2020); Zheng et al. (2015); Rakotondrandisa et al. (2020); Pan et al. (2021); Qaddah et al. (2022) for BDF and Yoon et al. (2020); Son & Park (2021); Seo et al. (2020) for CNAB. Therefore, we also provide a comparison of the current scheme with the semi-implicit BDF and CNAB schemes in the following tests. The semi-implicit BDF-2 and CNAB-2 schemes have been provided in the Appendix B for the sake of completeness.

3.1. Convergence rates

We first investigate the spatial and temporal convergence rates of the algorithm developed herein using a manufactured analytic solution to the heat transfer equation. Consider the rectangular domain $\overline{ABCD}$ as depicted in Fig. 2(a), $0 \leq x \leq 2$, $-1 \leq y \leq 1$ and the following analytical solution to Eqs. (1a) -(1c),

$$\begin{cases} u = 2\sin(\pi x)\cos(\pi y)\sin(2t), \\ v = -2\cos(\pi x)\sin(\pi y)\sin(2t), \\ p = 2\sin(\pi x)\sin(\pi y)\cos(2t), \\ T = 2\cos(\pi x)\sin(\pi y)\sin(2t), \end{cases} \tag{40}$$

where velocity $\mathbf{u} = (u, v)$. In equations (1a) and (1c), the source terms $\mathbf{f}(\mathbf{x}, \mathbf{t})$ and $g(\mathbf{x}, t)$ are chosen such that the equations are satisfied by the expressions from (40).

The computational domain is discretized by two quadrilateral elements with the same size as shown in Fig. 2(a). We impose condition (4) and (5)on the domain boundary for the velocity field. For the temperature field, Dirichlet condition (6) is imposed on sides $\overline{AB}$, $\overline{AE}$, $\overline{ED}$ and $\overline{CD}$, and Neumann condition (7) is imposed on the sides $\overline{BF}$ and $\overline{FC}$. Both the boundary values for Dirichlet and Neumann conditions are chosen according to analytical expressions from (40). The

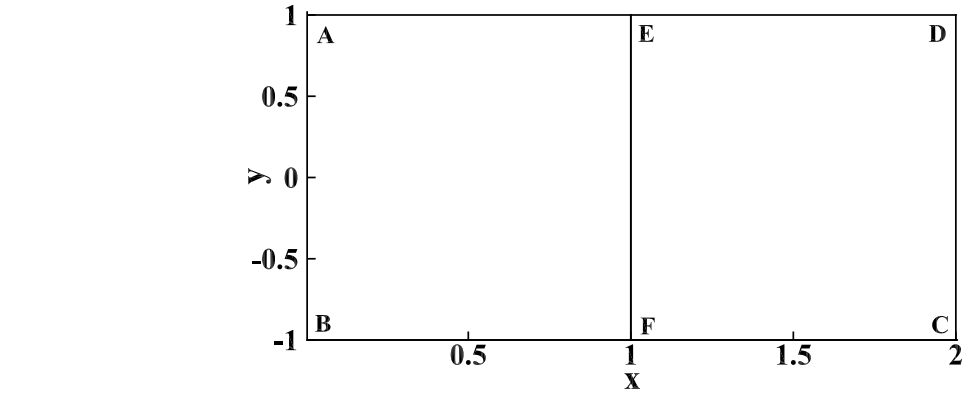

(a)

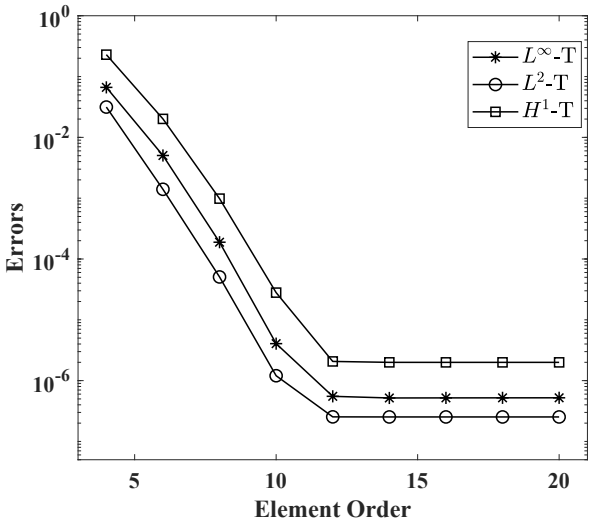

(b)

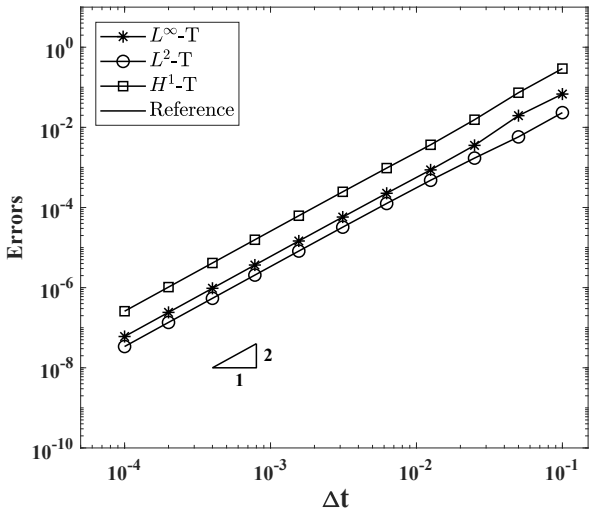

(c)

Figure 2 Convergence tests: (a) Flow domain and configuration; (b) Temperature errors (L^∞, L^2 and H^1 norms) vs. the element order (fixed $t_f = 0.1$ and Δt =0.001); (c) Temperature errors vs. time step size Δt (fixed $t_f = 0.5$ and element order 16).

initial velocity $\mathbf{u_{in}}$ and temperature T_{in} are chosen according to the analytical expressions from (40) by setting $t = 0$.

We integrate the heat transfer and Navier-Stokes equations in time from $t = 0$ to $t = t_f$ (to be specified later). The algorithm from Section 2 and Appendix A are used to solve the temperature and velocity fields, respectively. A fixed non-dimensional viscosity $\nu = 0.01$ and thermal diffusivity $\alpha = 0.01$ are chosen for the problem. Other parameters include the constant $C_0 = 1.0$ in Eq. (12) and the constant integer $k_0 = 1$ in Eq. (16). To test the spatial and temporal convergence behavior of the proposed algorithm, we have varied the element order and time step size systematically, and computed the corresponding errors in the L^∞, L^2 and H^1 norms.

Fig. 2(b) illustrates the spatial convergence behavior of the proposed method. We employ fixed

$t_f = 0.1$ and $\Delta t = 0.001$, and vary the element order between 4 and 20 in the simulations. This figure shows the temperature errors in L^∞, L^2 and H^1 norms at $t = t_f$ as a function of the element order. With increasing element order, a clear exponential decrease in the errors is observed for the element orders 12 and below. As the element order increases over 12, an error saturation is observed, owing to the dominance of temporal truncation errors.

Fig. 2(c) illustrates the behavior of the method for temporal convergence tests. We fix the element order 16 and $t_f = 0.5$, and vary the time step size between $\Delta t = 0.1$ to $\Delta t = 0.0001$. The figure shows the L^∞, L^2 and H^1 errors at $t = t_f$ as a function of Δt. It is evident that the scheme exhibits a second-order convergence rate in time for the temperature.

3.2. Flow past a warm circular cylinder

In this section, we test the proposed unconditional energy stable scheme using a canonical problem, the heat transfer in the flow past a warm circular cylinder.

We first compare our simulations with previous studies Bharti et al. (2007); Zhang et al. (2008) to verify the accuracy of the proposed method. Consider a flow domain depicted in Fig. 3(a), $-5d \leq x \leq 10d$, $-10d \leq y \leq 10d$, where d is the diameter of the circular cylinder and the cylinder center coincides with the origin of the coordinate system. On the left side of the domain, $\mathbf{u} = (1, 0)$ and $T = 0$ are prescribed. On the right side, an open boundary condition is imposed for the velocity field and a zero-normal derivative ($\mathbf{n} \cdot \nabla T = 0$) is specified for the temperature field. On the surface of the cylinder wall, we set $\mathbf{u} = (0, 0)$ and two kinds of boundary conditions for the temperature: $T = 1$ for the case of the constant wall temperature (CWT) and $\mathbf{n} \cdot \nabla T = -1$ for the case of the constant wall heat-flux (CWH). The top and bottom of the domain are assumed to be periodic. $U_0 = 1$, $d = 1$, and $T_d = 1$ degree Celsius are chosen as the velocity, length, and temperature scales, respectively, and all the physical variables and parameters are normalized accordingly.

For comparison, the convective heat transfer problem is performed under Reynolds number $Re = 20$ and Prandtl number $Pr = \nu/\alpha = 0.7$. We employ the scheme from Section 2 to simulate the temperature field with $g = 0$ in Eq. (1c), and use the algorithm in Appendix A to solve the Navier-Stokes equations (1a)- (1b) with $\mathbf{f} = \mathbf{0}$. We have meshed the domain into 1228 quadrilateral elements and employed element order 4, $\Delta t = 0.001$, $C_0 = 1000$ and $k_0 = 20$ for the simulations. The temperature distribution of the two cases are shown in Fig. 3(b) and 3(c). Fig. (4) demonstrates the distributions of the local Nusselt number Nu on the cylinder wall from the current simulation and from the previous works of (Bharti et al. (2007); Zhang et al. (2008)). The results evidently

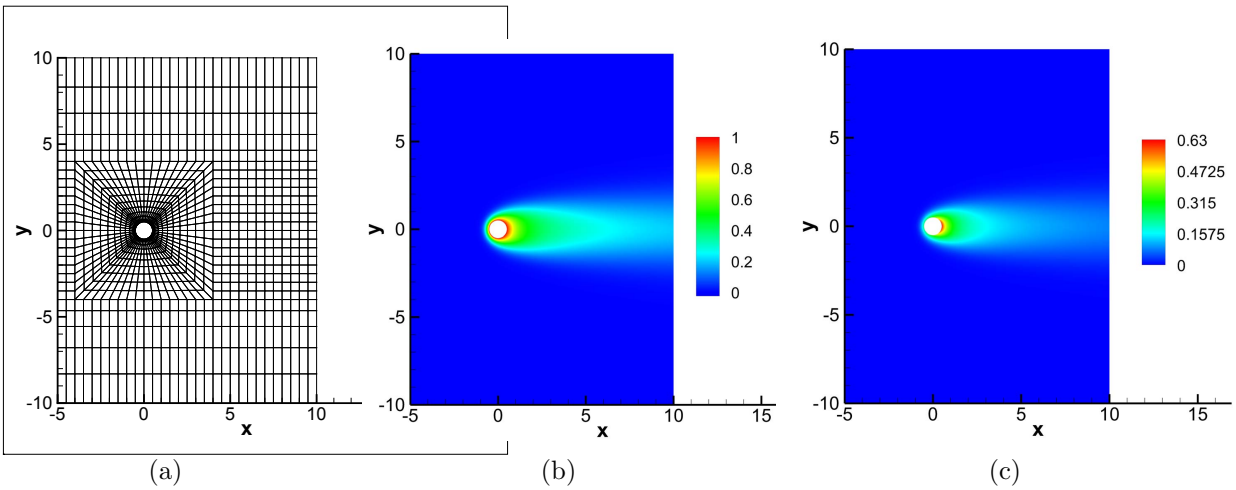

(a) (b) (c)

Figure 3 Circular cylinder flow: (a) Flow domain and mesh of 1228 quadrilateral elements; (b) Temperature distribution for constant wall temperature, $T = 1.0$; (c) Temperature distribution for constant wall heat flux, $\mathbf{n} \cdot \nabla T = -1$. Plots (b) and (c) are obtained at Reynolds number $Re = 20$ and $Pr = 0.7$.

show that our simulation results are in good agreement with those of (Bharti et al. (2007); Zhang et al. (2008)).

Let us next look into the performance of the proposed method. Consider the flow domain depicted in Fig. 5, $-2.5d \leq x \leq 6.5d$, $-1.5d \leq y \leq 1.5d$. The surface of the cylinder is set to be $T_h = 80$ degree Celsius. The top and bottom of the domain are the cooling walls, which are set to $\mathbf{n} \cdot \nabla T = 10.0$ and $T = 20.0$ respectively. The left and right sides are assumed to be periodic. A external force $\mathbf{f} = (2\nu, 0)$ is imposed on the domain to drive the flow. This configuration is equivalent to the flow past an infinite sequence of a warm circular cylinder in the horizonal direction.

We have discretized the domain using a mesh of 720 quadrilateral elements as shown in Fig. 5. No-slip condition for the velocity is imposed on the top, bottom and cylinder surface walls for the velocity field. The Dirichlet condition is employed for the bottom boundary with $T_d = 20$ degree Celsius and the cylinder surface with $T_h = 80$ degree Celsius. A Neumann condition with $g_c = 10$ in Eq. (7) is imposed on the top boundary. In addition, periodic conditions are imposed on the left and right boundaries for both temperature and velocity fields. We use the algorithm from Section 2 to simulate the temperature with $g = 0$ in Eq. (1c) and the algorithm in Appendix A to solve the Navier-Stokes equations (1a)- (1b) with a horizontal body force $\mathbf{f} = (2\nu, 0)$. Three Reynolds numbers ($Re = 100$, 500 and 3000) and three thermal diffusivity ($\alpha = 0.01$, 0.005 and 0.001) are chosen for numerical simulations. For each case, a long-time simulation is conducted such that the flow and temperature have reached a statistically stationary state, and thus the initial condition

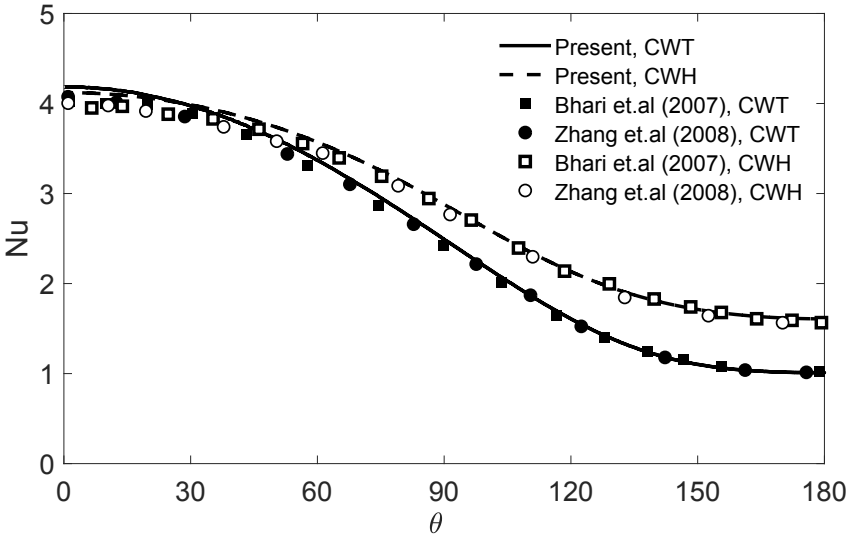

Figure 4 Circular cylinder flow: Comparisons of local Nusselt number distributions on the cylinder surface between the present work and previous work (Bharti et al. (2007); Zhang et al. (2008)) at Re = 20 and Pr = 0.7. θ is the angle defined in a sense of clockwise from 0 degree on point (-0.5, 0) to 180 degree on point (0.5, 0).

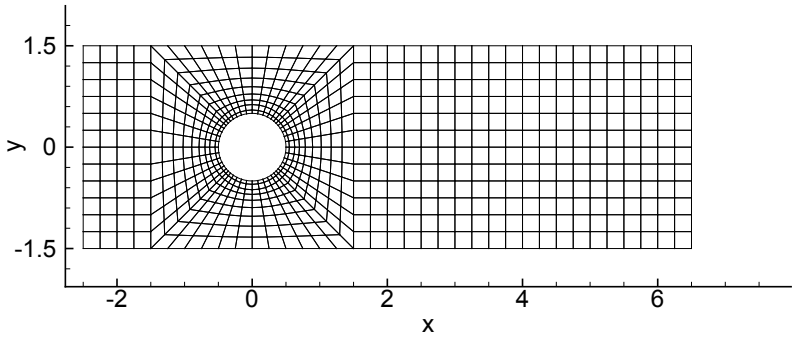

Figure 5 Circular cylinder flow: Domain configuration and the mesh of 720 quadrilateral elements

will have no effect on the presented results.

Fig. 6 provides an overview of the characteristic of the flow and temperature fields, which visualize the flow pattern (left column) and temperature distribution (right column) at Reynolds numbers $Re = 100$ (top row) and $Re = 500$ (bottom row) with the non-dimensional thermal diffusivity $\alpha = 0.01$. For $Re = 100$, the result is performed with an element order 4, a time step size $\Delta t = 0.01$. For $Re = 500$, the simulations is performed using an element order 6, a time step size $\Delta t = 0.005$. The parameters $C_0 = 1000$ and $k_0 = 1$ are employed for both cases. At the lower Reynolds number, i.e $Re = 100$, this is a steady flow. At Reynolds number $Re = 500$, the regular vortex shedding can be observed in the cylinder wake. Because of the periodicity, after the fluid passing through the warm cylinder, the warmed fluid re-enters the domain from the left side and

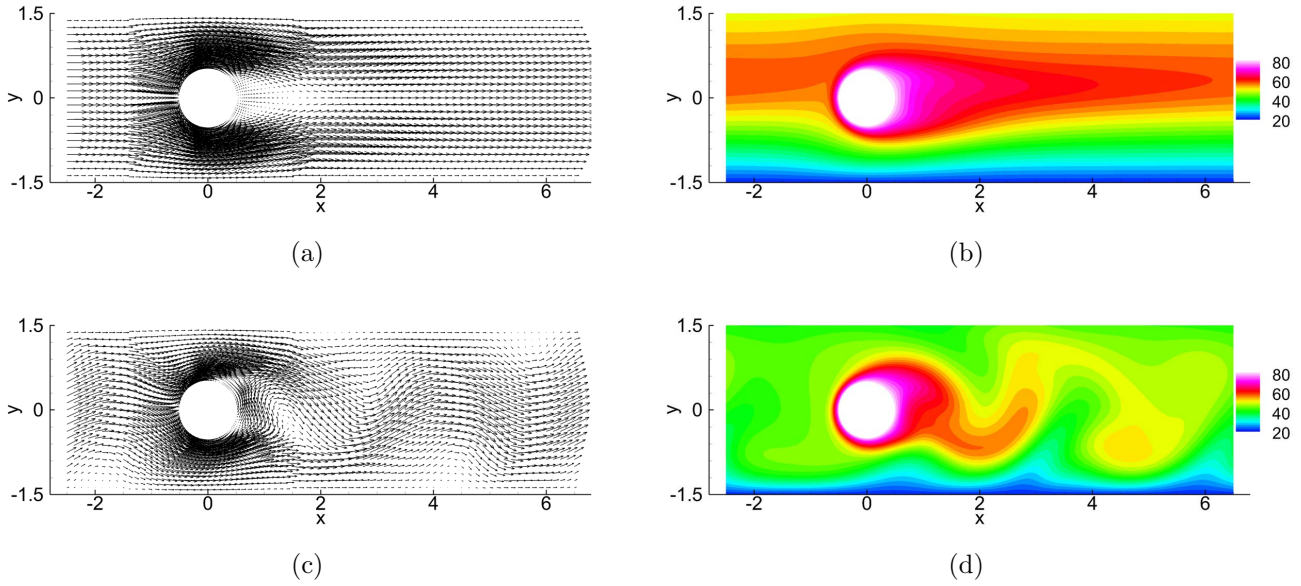

Figure 6 Circular cylinder flow: Instantaneous velocity and temperature distributions for $Re = 100$ (plots (a) and (b)) and $Re = 500$ (plots (c) and (d)) with thermal diffusivity $\alpha = 0.01$.

interacts with the cylinder.

To describe the overall evolution characteristic quantitatively, we have computed and monitored the $L2$ and $H1$ norms of the temperature field as following,

$$T_{L2}(t) = \sqrt{\frac{1}{V_\Omega}\int_\Omega [T(\mathbf{x},t)]^2 d\Omega}, \quad T_{H1}(t) = \sqrt{\frac{1}{V_\Omega}\int_\Omega \left[(T(\mathbf{x},t))^2 + |\nabla T|^2\right] d\Omega}, \tag{41}$$

where $V_\Omega = \int_\Omega d\Omega$ is the volume of the domain. Fig. 7 shows a window of the time histories of $T_{L2}(t)$ and $T_{H1}(t)$ at Reynolds numbers $Re = 500$ with a thermal diffusivity $\alpha = 0.01$. The simulation is performed using an element order 6, a time step size $\Delta t = 0.005$, $C_0 = 1000$ and $k_0 = 1$. A regular fluctuation in time is observed for both temperature norms. The $T_{H1}(t)$ exhibits a large magnitude, while the $T_{L2}(t)$ is much weaker in comparison. These time histories in the plot show a long-term stability of our simulations. It can be observed that the $T_{L2}(t)$ and $T_{H1}(t)$ fluctuate at some constant average level. Such invariable characteristics indicate that the temperature and velocity fields have reached a statistically stationary state.

Based on the time histories of $T_{L2}(t)$ and $T_{H1}(t)$, we can obtain the statistical quantities and compare them to test the effect of simulation parameters. The time-average mean value and root-mean-square (rms) value of $T_{L2}(t)$ and $T_{H1}(t)$ will be computed in the following simulations. In Table 1 we list the mean values ($\overline{T}_{L2}$ and $\overline{T}_{H1}$) and rms values (T'_{L2} and T'_{H1}) of $T_{L2}(t)$ and

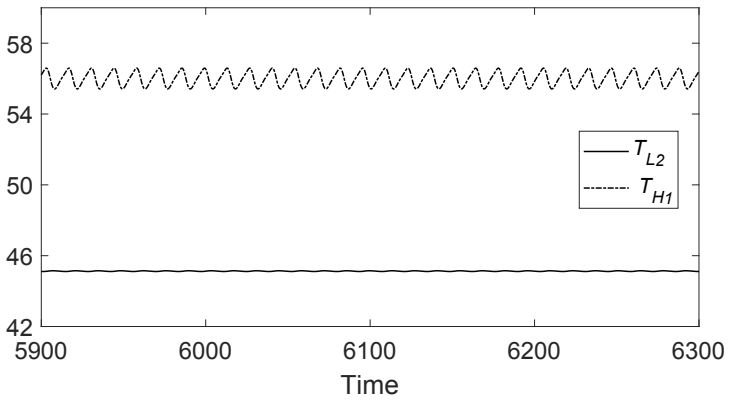

Figure 7 Circular cylinder flow: Time histories of $T_{L2}(t)$ and $T_{H1}(t)$ at Reynolds number $Re = 500$ with $\alpha = 0.01$

$T_{H1}(t)$ obtained using different element orders, for Reynolds number $Re = 100$, 500 and 3000 with thermal diffusivity $\alpha = 0.01$. The time step size is set as $\Delta t = 0.001$ for $Re = 100$ and $Re = 500$, and $\Delta t = 5e - 4$ for $Re = 3000$. In these simulations, fixed values of $C_0 = 1000$ and $k_0 = 1$ are employed. It is observed that the mean and rms values of temperature norms are basically the same for all the element orders, demonstrating a sense of convergence. In the results reported below, the simulations are performed using element order 4 for $Re = 100$ and element order 6 for $Re = 500$ and $Re = 3000$.

Table 1
Circular cylinder flow: Mean and rms values of $T_{L2}(t)$ and $T_{H1}(t)$ obtained with various element orders at three Reynolds numbers. Thermal diffusivity is $\alpha = 0.01$.

Reynolds number	Element order	$\overline{T}_{L2}$	T'_{L2}	$\overline{T}_{H1}$	T'_{H1}
100	2	50.909	0	57.874	0
	3	50.901	0	57.862	0
	4	50.901	0	57.861	0
	5	50.901	0	57.862	0
	6	50.901	0	57.862	0
500	3	45.106	1.48e-2	55.992	0.398
	4	45.127	1.46e-2	55.996	0.397
	5	45.128	1.46e-2	55.995	0.397
	6	45.128	1.46e-2	56.002	0.397
	7	45.128	1.46e-2	56.002	0.397
3000	3	43.786	0.591	53.634	0.904
	4	43.729	0.589	53.600	0.824
	5	43.753	0.529	53.593	0.815
	6	43.619	0.546	53.577	0.849
	7	43.650	0.510	53.522	0.816

Let us next focus on the effect of the time step size on accuracy and stability of the simulation results. Note that in the previous simulations, the time step size used for solving velocity and temperature fields are the same. To eliminate the effect of the velocity time step sizes on simulation results, we fix them at constant values in all the simulations below and solve the temperature field at every N-th time step of the velocity, where N is an integer given by users. Here, we denote Δt_V as the velocity time step size and Δt_T as the temperature time step size. The relationship of the two time step sizes can be given as $\Delta t_T = N \times \Delta t_V$. It is worth noting that in such cases, the velocity field $\mathbf{u_0}$ will be updated at every $N \times k_0$ velocity time step instead of at every k_0 velocity time step.

Table 2 lists the mean and rms values of the temperature norms computed using current scheme with temperature time step size ranging from $\Delta t_T = 0.01$ to $\Delta t_T = 100$. We also perform the same simulations with the semi-implicit methods i.e. second-order back forward formula (BDF-2) and Crank-Nicolson Adam-Bashforth (CNAB-2) methods for comparison. The details of the two semi-implicit methods are gathered in Appendix B. In these simulations, the velocity time step sizes are given as $\Delta t_V = 0.01$, 0.005 and 0.001 for the tests corresponding to Reynolds numbers $Re = 100$, 500 and 3000 respectively. Fixed $C_0 = 1000$ and $k_0 = 1$ are employed for all the cases. The thermal diffusivity is $\alpha = 0.01$ for Reynolds number $Re = 100$ and 500, and $\alpha = 0.001$ for $Re = 3000$. We observe that current method can produce stable results even at a very large time step size. Moreover, at lower Reynolds number, see $Re = 100$, the accuracy results can be obtained even at $\Delta t_T = 100$, while the semi-implicit method is ineffective once the Δt_T increases to 0.04.

For the higher Reynolds numbers, the simulations with current scheme seem to lose accuracy at a very large Δt_T, see the cases $\Delta t_T = 2.5$ and larger for $Re = 500$ and the cases $\Delta t_T = 5.0$ and larger for $Re = 3000$. To clarify the effect of the time step size, we plot the time history of the simulations for two higher Reynolds numbers, as demonstrated in Fig. 8 and Fig. 9. It can be observed that the accuracy of the results can be obtained even at $\Delta t_T = 0.5$ for $Re = 500$ with $\alpha = 0.01$ and $\Delta t_T = 1.0$ for $Re = 3000$ with $\alpha = 0.001$. For these cases for $Re = 500$ based on the semi-implicit methods, the effective results can only be obtained below $\Delta t_T = 0.05$ for the BDF-2 method and below $\Delta t_T = 0.025$ for the CNAB-2 method. As shown in Table 2, the main drawback of the traditional semi-implicit method is its conditional stability. A stable computation can be achieved only when the time step is small enough.

Since the velocity time step size is fixed, the calculated CFL numbers for each Reynolds number

flow are same, i.e. CFL = 1.70 for Reynolds number $Re = 100$, CFL = 1.25 for Reynolds number Re= 500, and CFL = 0.178 for Reynolds number $Re = 3000$. Therefore, we introduce an effective CFL number, $(\mathrm{CFL})_T$, which is defined in terms of the temperature time step size. As shown in Table 2, the accurate results with current method can be obtained even at a very large $(\mathrm{CFL})_T$, which is $(\mathrm{CFL})_T$=17000 for $Re = 100$ and $(\mathrm{CFL})_T$=89 for $Re = 3000$. At the same time, the semi-implicit method shows its weakness, where the acceptable $(\mathrm{CFL})_T$ is much smaller, i.e., $(\mathrm{CFL})_T$T = 3.4 for $Re = 100$ and $(\mathrm{CFL})_T$= 1.78 for $Re = 3000$. The proposed method demonstrates an effective way to extend the range of both accuracy and stability, as is evident from the results above.

Table 2
Circular cylinder flow: $(\mathrm{CFL})_T$, mean and rms values of $T_{L2}(t)$ and $T_{H1}(t)$ computed using a range of temperature time step sizes at three Reynolds numbers and two thermal diffusivity for several solvers.

Re	α	Method	Δt_T	$(\mathrm{CFL})_T$	$\overline{T}_{L2}$	T'_{L2}	$\overline{T}_{H1}$	T'_{H1}
100	0.01	Current	0.01	1.7	50.901	0	57.862	0
			0.1	17	50.902	0	57.862	0
			1	170	50.902	0	57.862	0
			10	1700	50.902	0	57.862	0
			100	17000	50.902	0	57.862	0
		Semi-implicit BDF-2	0.01	1.7	50.901	0	57.862	0
			0.02	3.4	50.901	0	57.862	0
			0.04	6.8	**blow up**			
		Semi-implicit CNAB-2	0.01	1.7	50.901	0	57.862	0
			0.02	3.4	50.901	0	57.862	0
			0.04	6.8	**blow up**			
500	0.01	Current	0.005	1.25	45.128	1.46e-2	55.998	0.397
			0.1	12.5	45.123	1.45e-2	55.995	0.395
			0.25	31.25	45.103	1.44e-2	55.975	0.397
			0.5	62.5	45.039	1.37e-2	55.887	0.387
			2.5	312.5	45.874	6.16e-3	55.266	0.208
			5	625	47.548	3.85e-3	55.582	0.104
			25	3125	49.581	8.32e-2	57.006	0.163
		Semi-implicit BDF-2	0.005	1.25	45.127	1.46e-2	56.000	0.396
			0.05	12.5	45.130	1.46e-2	55.997	0.396
			0.1	25	**blow up**			
		Semi-implicit CNAB-2	0.005	1.25	45.128	1.46e-2	56.000	0.397
			0.025	6.25	45.128	1.46e-2	56.000	0.396
			0.05	12.5	**blow up**			
3000	0.001	Current	0.001	0.178	46.488	0.305	65.689	1.653
			0.025	4.45	46.490	0.304	65.694	1.652
			0.05	8.9	46.489	0.304	65.693	1.652
			0.1	17.8	46.488	0.304	65.690	1.650
			0.5	89	46.542	0.336	65.417	1.637
			1	178	46.427	0.338	64.876	1.527
			5	890	46.592	0.364	62.858	1.032
			10	1780	47.577	0.547	62.057	0.905
			50	8900	50.357	1.569	61.767	1.277
		Semi-implicit BDF-2	0.001	0.178	46.016	0.302	65.489	1.743
			0.01	1.78	45.910	0.387	65.447	1.639
			0.02	3.56	**blow up**			
		Semi-implicit CNAB-2	0.001	0.178	46.004	0.367	65.502	1.674
			0.01	1.78	45.943	0.408	65.627	1.822
			0.02	3.56	**blow up**			

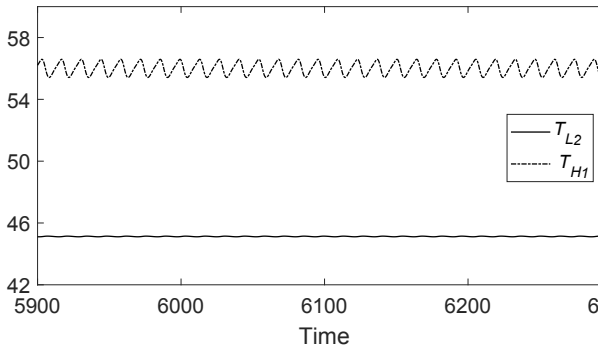

(a) $\Delta t_T = 0.005$

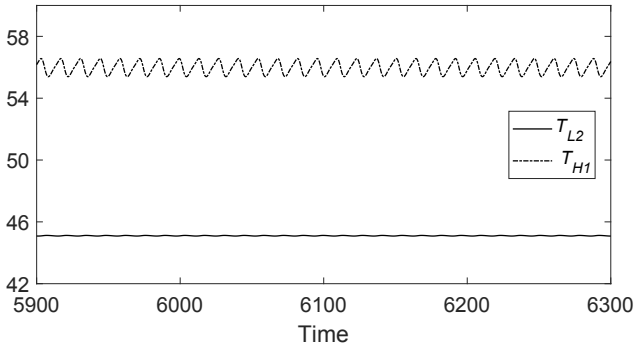

(b) $\Delta t_T = 0.25$

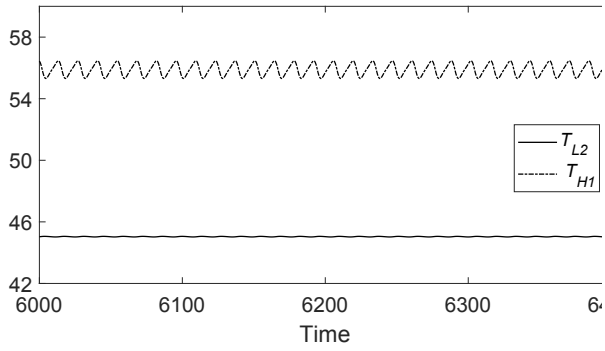

(c) $\Delta t_T = 0.5$

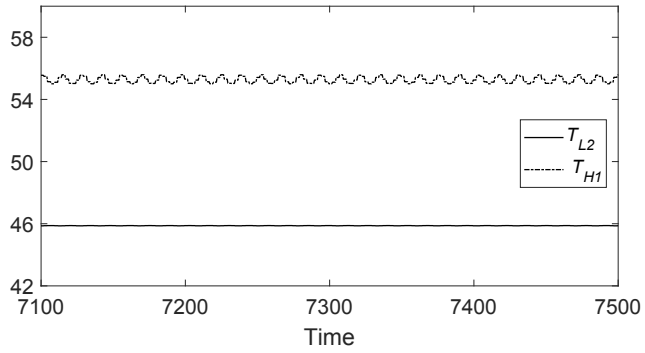

(d) $\Delta t_T = 2.5$

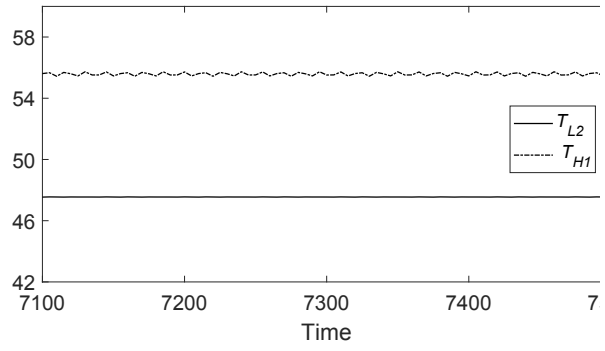

(e) $\Delta t_T = 5$

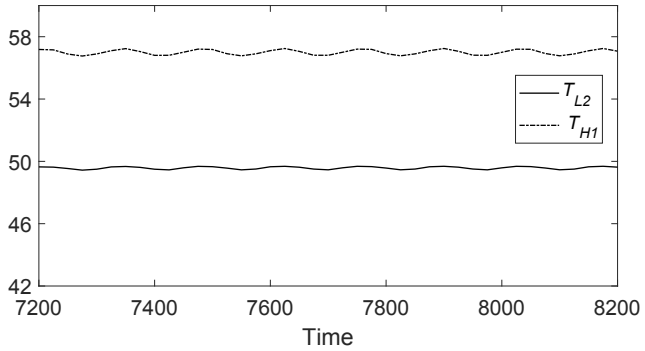

(f) $\Delta t_T = 25$

Figure 8 Circular cylinder flow: Time histories of the T_{L2} and T_{H1} at $Re = 500$ with $\alpha = 0.01$ obtained with different time step sizes Δt_T.

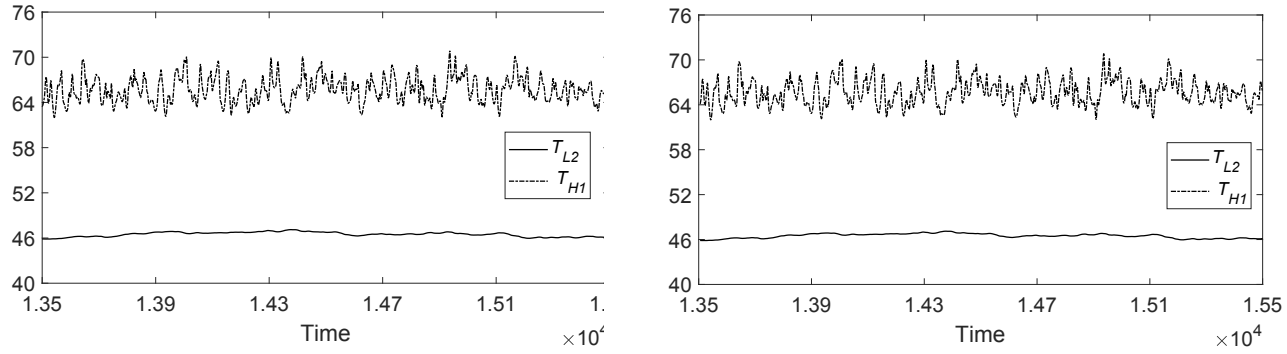

(a) $\Delta t_T = 0.001$

(b) $\Delta t_T = 0.1$

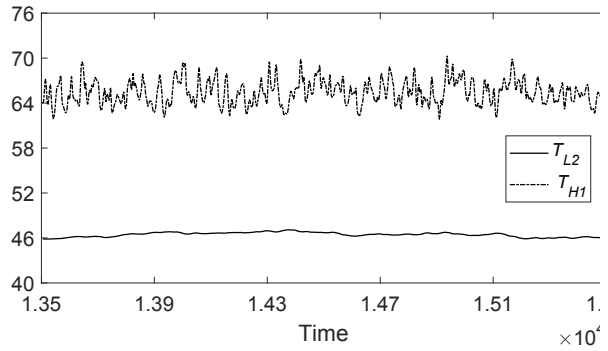

(c) $\Delta t_T = 0.5$

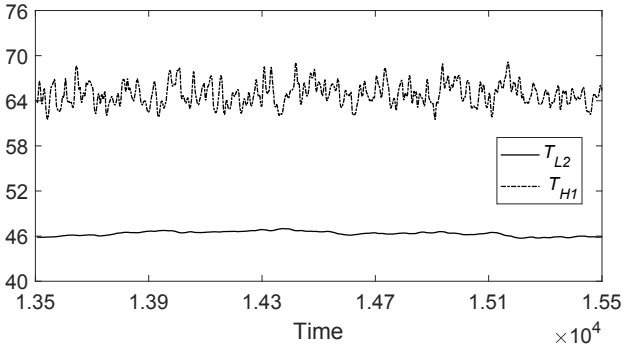

(d) $\Delta t_T = 1.0$

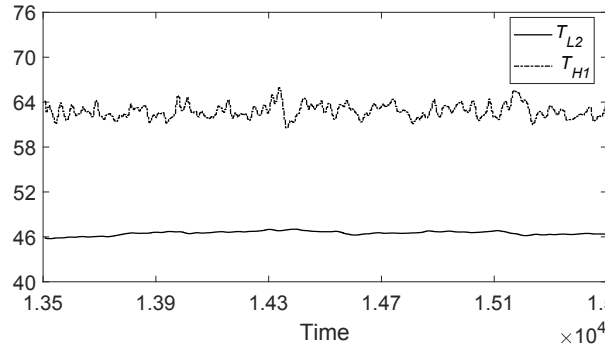

(e) $\Delta t_T = 5.0$

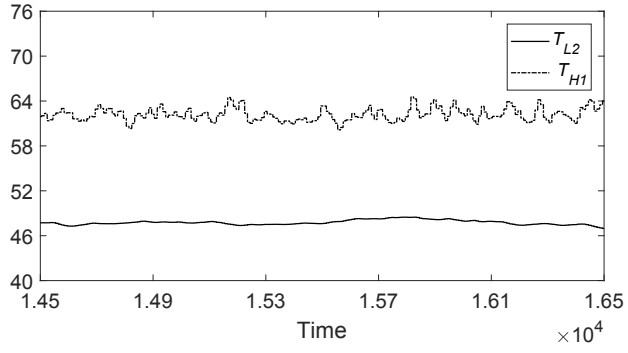

(f) $\Delta t_T = 10$

Figure 9 Circular cylinder flow: Time histories of the T_{L2} and T_{H1} at $Re = 3000$ with $\alpha = 0.001$ obtained with different time step sizes Δt_T.

In the presented method, the velocity field $\mathbf{u_0}$ is updated at every $N \times k_0$ velocity time step, leading to a periodically updating of the temperature coefficient matrix. We observe that the frequency for updating $\mathbf{u_0}$ has an impact on the accuracy of the simulation results. Note that the frequency is influenced by two factors, N and k_0. When the time step size of velocity Δt_V is fixed, the larger Δt_T means a larger N. Table 2 can also be seen as the effectiveness tests of N on the accuracy of the simulations, which shows that a too large N can cause an accuracy degradation.

We observe that with a too large k_0, the simulation results can also lose accuracy. Note that for the steady flow, once the velocity field reaches its steady state, the value of k_0 can not cause an effect on accuracy. It is because that the velocity field will not change with time. Therefore, in the following tests, the simulations corresponding to higher Reynolds numbers are mainly conducted.

Table 3 provides the mean and rms values of the temperature norms at Reynolds number $Re = 500$ with thermal diffusivity $\alpha = 0.01$ and 0.005, and $Re = 3000$ with $\alpha = 0.001$. In this set of simulations, we have employed $\Delta t_V = 5e-3$ for $Re = 500$ and $\Delta t_V = 1e-3$ for $Re = 3000$. Element order 6 and $C_0 = 1000$ are employed for all cases. We vary the constants k_0 and N (Δt_T) systematically to demonstrate the effect of the two parameters on the accuracy. It can be observed that with the increase of k_0, the accuracy of the simulation based on a large Δt_T shows an apparent decrease. For example, for $Re = 500$, when k_0 increases to 20, the accuracy starts to deteriorate at time step size $\Delta t_T = 0.5$; while for the case of $k_0 = 1$, a accurate result can also be maintained. This kind of accuracy deterioration is far more serious than the situation of a very large time step as shown in Fig. 8 and 9. This point is also demonstrated by Fig. 10 and 11, which show time histories of the temperature norms with $\mathbf{u_0}$ updated with different frequency. For $Re = 3000$, when k_0 increases to 10, the characteristics of the computed temperature norms at $\Delta t_T = 0.5$ becomes notably different from the accurate result. At this case, the velocity field $\mathbf{u_0}$ is updated at every 5000 velocity time steps. These results imply that, when $\mathbf{u_0}$ is updated too rarely, the correction term $(M(\mathbf{u_0}, T) - N(\mathbf{u}, T))$ may become very large and thus causes a significant error in simulations.

Table 3
Circular cylinder flow: Mean and rms values of $T_{L2}(t)$ and $T_{H1}(t)$ computed using a range of temperature time step sizes at Reynolds numbers $Re = 500$ with $\alpha = 0.01$ and 0.005 and $Re = 3000$ with $\alpha = 0.001$.

Re	α	k_0	Δt_T	$\overline{T}_{L2}$	T'_{L2}	$\overline{T}_{H1}$	T'_{H1}
500	0.01	1	0.005	45.128	1.46e-2	55.998	0.397
			0.1	45.123	1.45e-2	55.995	0.395
			0.25	45.103	1.44e-2	55.975	0.397
			0.5	45.039	1.37e-2	55.887	0.387
		10	0.005	45.128	1.46e-2	56.000	0.397
			0.1	45.122	1.45e-2	55.996	0.396
			0.25	45.088	1.43e-2	55.965	0.392
			0.5	44.944	1.32e-2	55.832	0.369
		20	0.005	45.128	1.46e-2	56.999	0.397
			0.1	45.121	1.46e-2	55.996	0.397
			0.25	45.072	1.42e-2	55.945	0.389
			0.5	46.039	2.28e-2	57.605	**3.768**
	0.005	1	0.005	45.931	8.59e-3	58.989	0.520
			0.05	45.929	8.58e-3	58.985	0.519
			0.25	45.886	8.31e-3	58.925	0.501
			0.5	45.795	7.62e-3	58.722	0.451
		5	0.005	45.931	8.59e-3	58.989	0.520
			0.05	45.929	8.56e-3	58.988	0.518
			0.25	45.877	8.29e-3	58.924	0.497
			0.5	45.730	7.44e-3	58.785	0.438
		10	0.005	45.931	8.59e-3	58.989	0.520
			0.05	45.929	8.58e-3	58.988	0.519
			0.25	45.864	8.24e-3	58.924	0.492
			0.5	45.855	8.58e-3	59.575	**1.636**
3000	0.001	1	0.001	46.488	0.305	65.689	1.653
			0.1	46.488	0.304	65.690	1.650
			0.5	46.542	0.336	65.417	1.637
			1	46.427	0.338	64.876	1.527
		5	0.001	46.594	0.337	65.661	1.698
			0.1	46.591	0.336	65.657	1.696
			0.5	46.527	0.334	65.488	1.651
			1	46.446	0.347	66.842	**8.963**
		10	0.001	46.594	0.337	65.661	1.698
			0.1	46.591	0.336	65.656	1.696
			0.5	46.644	0.353	67.199	**14.540**

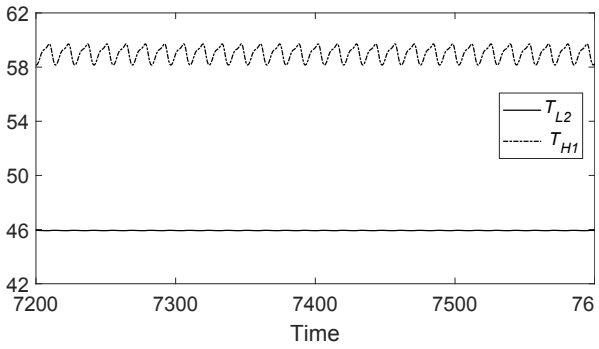

(a) $k_0 = 10, \Delta t_T = 0.005$

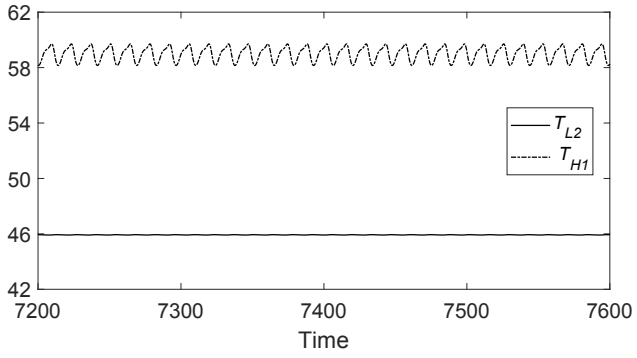

(b) $k_0 = 10, \Delta t_T = 0.1$

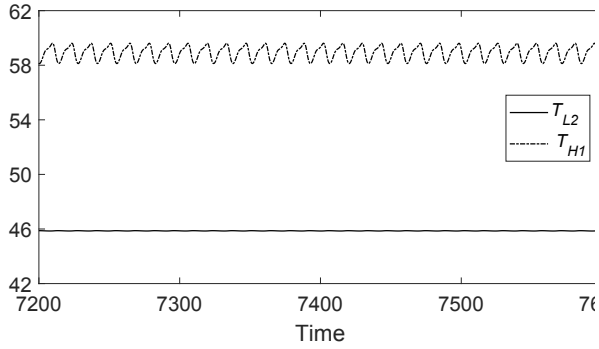

(c) $k_0 = 10, \Delta t_T = 0.25$

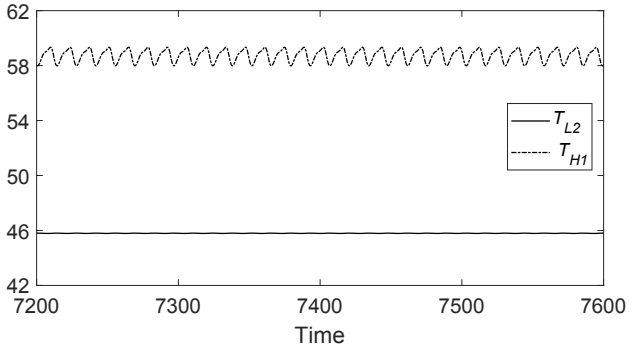

(d) $k_0 = 1, \Delta t_T = 0.5$

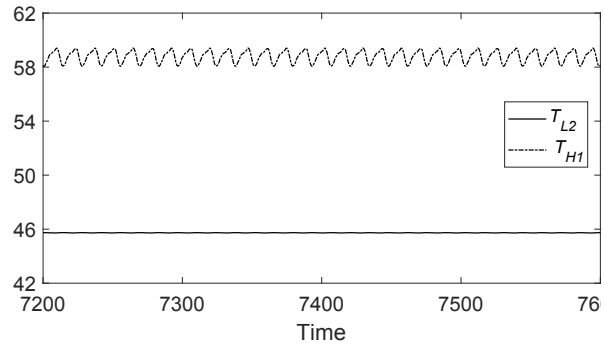

(e) $k_0 = 5, \Delta t_T = 0.5$

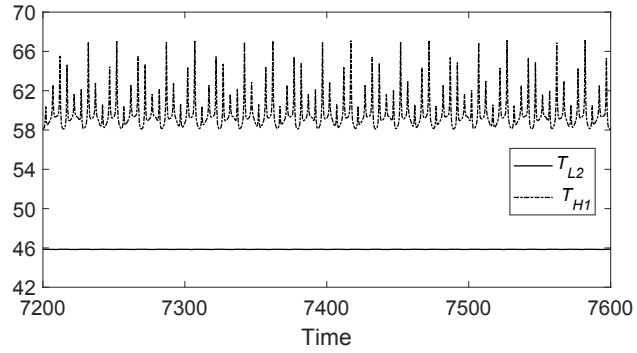

(f) $k_0 = 10, \Delta t_T = 0.5$

Figure 10 Circular cylinder flow: Time histories of the T_{L2} and T_{H1} at Reynolds number $Re = 500$ with thermal diffusivity $\alpha = 0.005$, obtained using a range of k_0 values and time step sizes Δt_T.

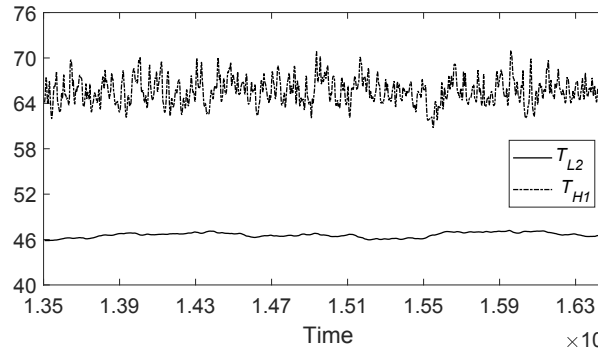

(a) $k_0 = 5, \Delta t_T = 0.001$

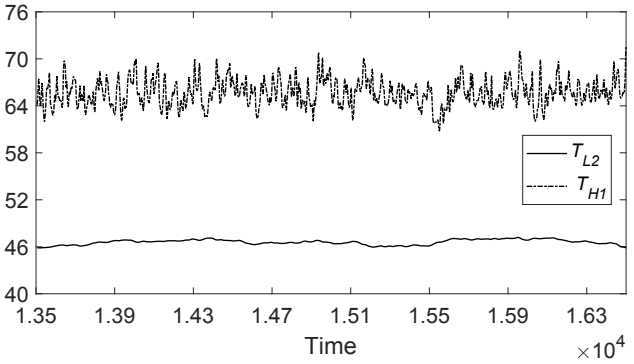

(b) $k_0 = 5, \Delta t_T = 0.1$

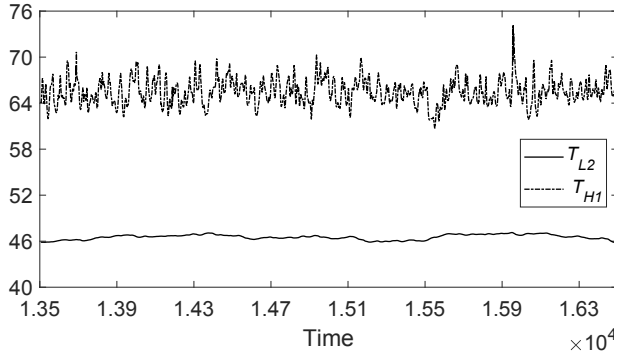

(c) $k_0 = 5, \Delta t_T = 0.5$

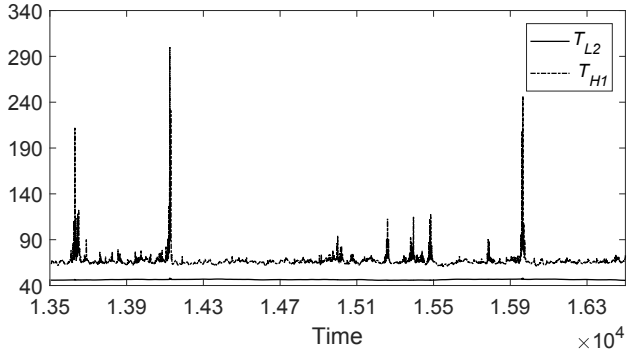

(d) $k_0 = 5, \Delta t_T = 1.0$

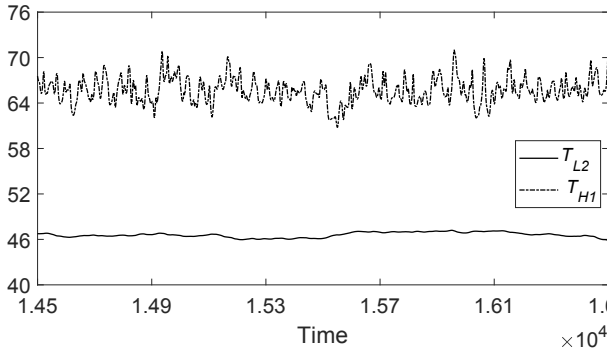

(e) $k_0 = 10, \Delta t_T = 0.001$

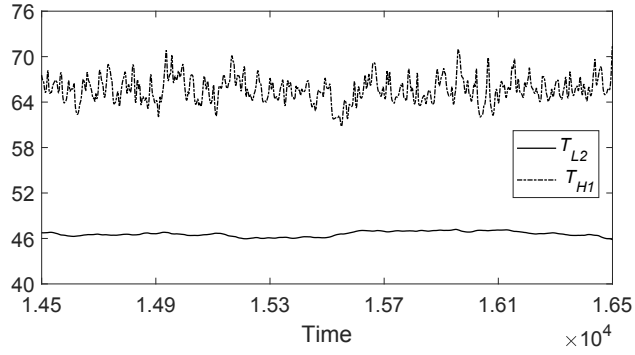

(f) $k_0 = 10, \Delta t_T = 0.1$

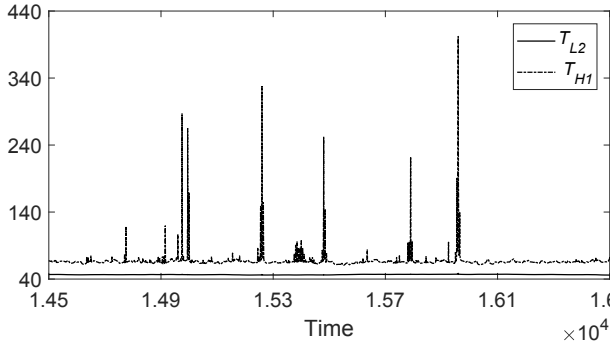

(g) $k_0 = 10, \Delta t_T = 0.5$

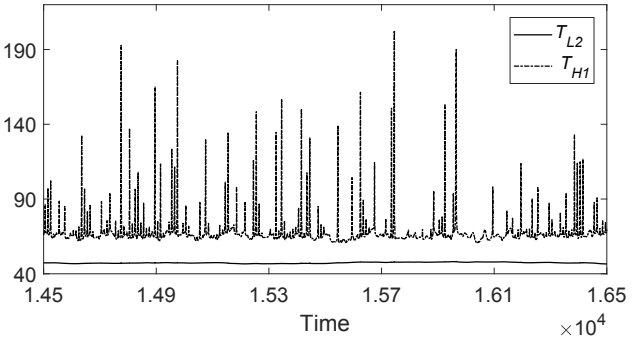

(h) $k_0 = 10, \Delta t_T = 1.0$

Figure 11 Circular cylinder flow: Time histories of the T_{L2} and T_{H1} at Reynolds number $Re = 3000$ with $\alpha = 0.001$, obtained with different frequency parameter k_0 and time step sizes Δt_T.

We can also utilize a modified scheme with $M(\mathbf{u_0}, T) = 0$ to simulate the convective heat transfer problem. Note that for the modified scheme, the same algorithm presented by Eqs.(21a)-(22) can be used and the energy stable property still holds on. The modification shows an advantage in the computational cost, since the discretized linear systems only involve the constant and time-independent coefficient metrics and can be pre-computed. However, the modified method shows a lower accuracy and robustness compared with the presented scheme when the time step size increases to a fairly large values.

Table 4 provides the mean and rms values of temperature norms at $Re = 100$ with $\alpha = 0.01$ obtained with the modified scheme. Element order 4 and $\Delta t_V = 0.01$ is employed for the simulations, and the constant C_0 and time step size Δt_T are varied systematically. This table can be compared with Table 2, in which the results are attained by using current method and the accurate results can be obtained even at $\Delta t_T = 100$. It can be observed that the modified scheme can provide stable results at large time step sizes, however, the accuracy range of the simulations is reduced and significantly influenced by C_0. Table 5 demonstrates the effect of C_0 on the accuracy of simulation results using the current method. These simulations are performed with element order 4, $\Delta t_V = 0.01$, $\Delta t_T = 0.05$ and $k_0 = 20$. We observe that the computed results are the same corresponding to different C_0 values. This suggests that our method has a low sensitivity to C_0, showing a superior accuracy and robustness to the modified method. Since the current method is not quite sensitive to C_0, choosing the C_0 value is largely a preference of the user. In practice, we recommend using a small C_0 such as 1 or 10 for low Reynolds numbers and a relatively larger C_0 such as 1e3 or 1e6 for higher Reynolds numbers.

Table 4
Circular cylinder flow: Mean and rms values of $T_{L2}(t)$ and $T_{H1}(t)$ using a range of C_0 and temperature time step size at Reynolds number $Re = 100$ with modified scheme $M(\mathbf{u_0}, T) = 0$. Thermal diffusion is $\alpha = 0.01$.

C_0	Δt_T	$\overline{T}_{L2}$	T'_{L2}	$\overline{T}_{H1}$	T'_{H1}
1	0.01	50.899	0	57.859	0
	0.02	50.899	0	57.859	0
	0.05	50.461	1.95e-2	58.109	2.220
1e3	0.01	50.899	0	57.859	0
	0.02	50.898	0	57.859	0
	0.05	50.527	8.87e-2	57.807	**4.973**
1e9	0.01	50.901	0	57.862	0
	0.02	50.901	0	57.862	0
	0.05	49.729	0	56.670	0

Table 5
Circular cylinder flow: Mean and rms values of $T_{L2}(t)$ and $T_{H1}(t)$ using a range of C_0 at Reynolds number $Re = 100$ and time step size $\Delta t_T = 0.05$ with current method. Thermal diffusion is $\alpha = 0.01$.

C_0	$\overline{T}_{L2}$	T'_{L2}	$\overline{T}_{H1}$	T'_{H1}
1e-3	50.902	0	57.862	0
1	50.902	0	57.862	0
1e3	50.902	0	57.862	0
1e9	50.901	0	57.862	0

Fig. 12 and 13 show a temporal sequence of the velocity and temperature fields at the Reynolds number $Re = 3000$ and a non-dimensional thermal diffusivity $\alpha = 0.001$. Here, we have employed element order 6, $C_0 = 1000$ and $k_0 = 1$. A time step $\Delta t = 0.001$ is used for solving both temperature and velocity fields. It can be observed that strong vortices generate at the warm cylinder and shed into the wake. Besides, due to the periodicity, the vortices contained warm fluid pass through the right boundary and go into the upstream of the domain. Then the re-entered flow interacts with the warm cylinder and generates complex heat and fluid dynamics.

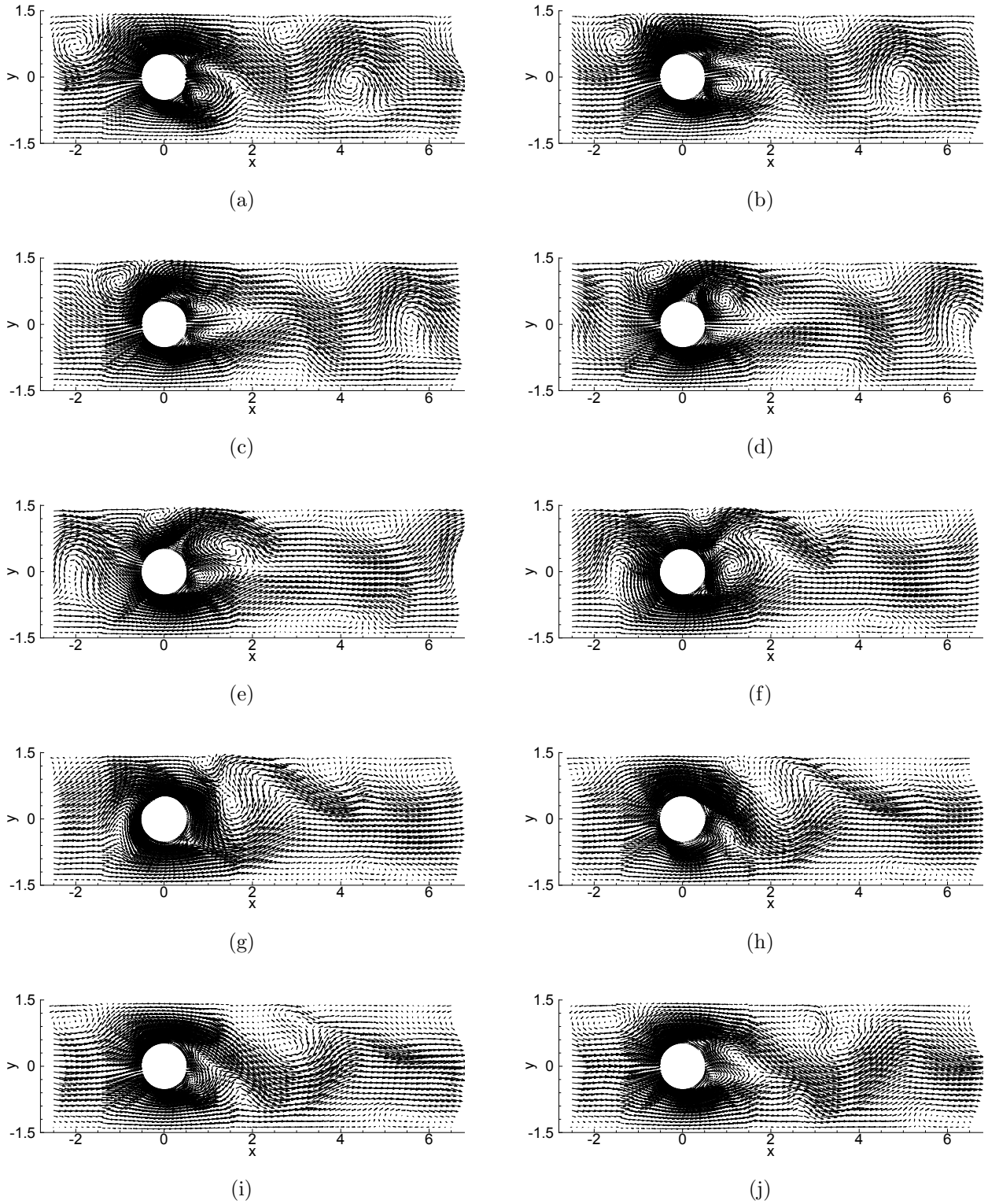

Figure 12 Circular cylinder flow: Temporal sequence of snapshots of the velocity fields at Reynolds number $Re = 3000$, (a) $t = t_0$, (b)$t = t_0 + 6.4$, (c) $t = t_0 + 12.8$, (d)$t = t_0 + 19.2$, (e) $t = t_0 + 25.6$, (f) $t = t_0 + 32.0$, (g) $t = t_0 + 38.4$, (h) $t = t_0 + 44.8$, (i) $t = t_0 + 51.2$, (j) $t = t_0 + 57.6$. t_0 denotes the initial time instance of the sequence.

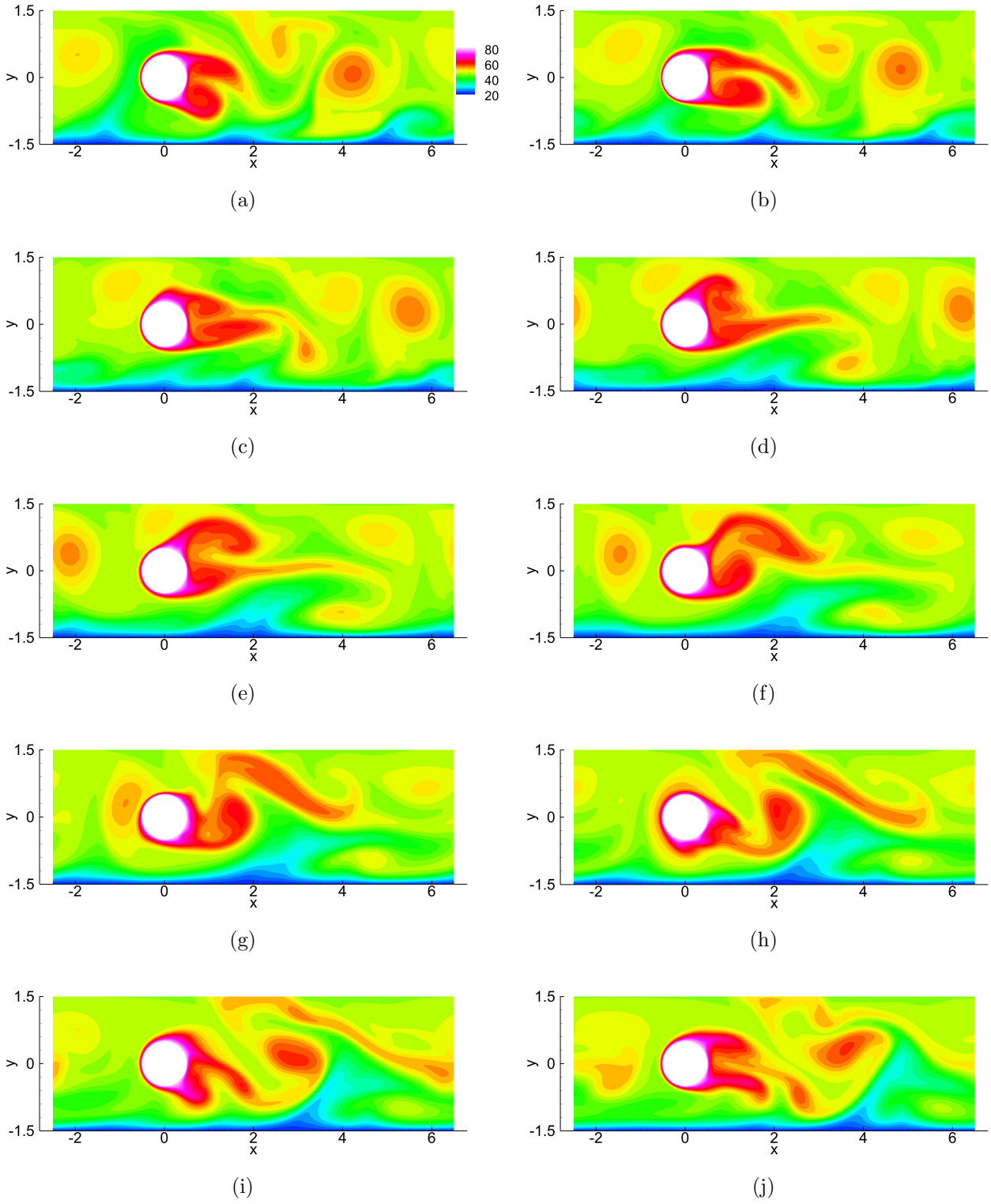

Figure 13 Circular cylinder flow: Temporal sequence of snapshots of the temperature field at Reynolds number $Re = 3000$ and thermal diffusivity $\alpha = 0.001$, at identical time instance as in Fig. 12, (a) $t = t_0$, (b)$t = t_0 + 6.4$, (c) $t = t_0 + 12.8$, (d)$t = t_0 + 19.2$, (e) $t = t_0 + 25.6$, (f) $t = t_0 + 32.0$, (g) $t = t_0 + 38.4$, (h) $t = t_0 + 44.8$, (i) $t = t_0 + 51.2$, (j) $t = t_0 + 57.6$.

3.3. Flow past a warm square cylinder in a T-shaped periodical channel

In this subsection we test the accuracy and stability of the presented scheme by simulating another canonical convective heat transfer problem in two dimensions, flow past a warm square cylinder in a T-shape periodical channel.

Specifically, we consider a domain depicted in Fig. 14. A square cylinder with a length of side 0.5 is mounted on the center of the channel, and the cylinder center coincides with the point (1, 0). A horizontal body force of normalized magnitude $|\mathbf{f}| = 200\nu$ is imposed on the domain and drives the flow. The boundaries of the domain in the horizontal direction ($x = 0, 2$) are assumed periodic. All the rest of the boundaries are walls. The surface of the cylinder is maintained at $T_h = 80$ degrees Celsius. The top wall is set at $T_l = 20$ degrees Celsius. A fixed heat-flux $\mathbf{n} \cdot \nabla T = 10$ is imposed on the bottom walls of the domain. This configuration mimics the flow past an infinite array of a square cylinder in the horizontal direction. We choose the height of the channel ($-0.5 < x < 0.5$) as the length scale, $U_0 = 1$ as the velocity scale and $T_d = 1$ degree Celsius as the temperature scale. All the other physical variables and parameters are then normalized accordingly.

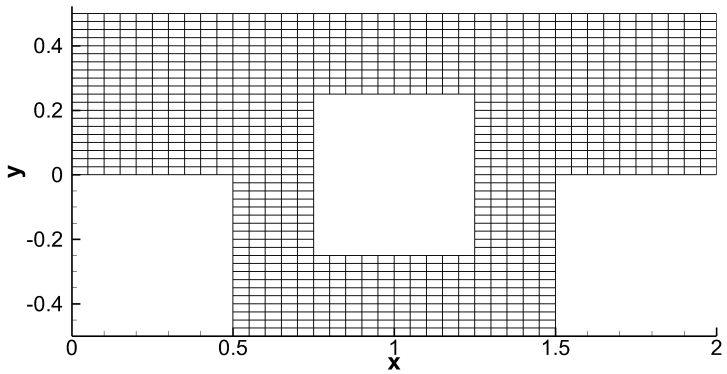

Figure 14 Square cylinder flow: Flow domain and the mesh of 1000 quadrilateral elements

We discretise the domain using a mesh of 1000 quadrilateral elements as shown in Fig. 14. On the top and bottom of the domain, and on the surface of the square cylinder, no-slip boundary conditions are imposed for the velocity field. For the temperature field, we impose Dirichlet boundary condition with $T_l = 20$ and $T_h = 80$ on the top wall and on the surface of the cylinder. Neumann boundary condition is imposed on the bottom walls as mentioned before. Periodic conditions are imposed on the left and right boundaries for all field variables. The algorithm from Section 2 is employed to solve the temperature field with $g = 0$. The Navier-Stokes equations with a horizontal body force $\mathbf{f} = (200\nu, 0)$, are solved using the algorithm in Appendix A. We have conducted the simulations for three Reynolds numbers (Re = 300, 1000, and 5000) and two

Peclet numbers (corresponding to thermal diffusivity $\alpha = 0.01$ and 0.001). The effect of parameters including element order, time step size, and k_0 on the heat transfer characteristics are systematically investigated.

An overview of the flow and heat transfer characteristics of this problem is provided by Fig. 15, which visualize the flow pattern using streamlines and temperature distribution at two Reynolds numbers $Re = 300$ and 1000 with thermal diffusivity $\alpha = 0.01$. These results are computed using element order 6 and $C_0 = 1000$ for $Re = 300$, and element order 7 and $C_0 = 1e9$ for $Re = 1000$. The parameters $\Delta t = 5e-4$, $k_0 = 20$ are employed for both cases. At low Reynolds number, i.e., $Re = 300$, one observes a steady flow. As the Reynolds number increases to $Re = 1000$, it can be seen that the length of vortices near the walls becomes larger. The vortices flow past the right side of the domain and then re-enter the upstream of the cylinder, which further influences the temperature distribution of the domain.

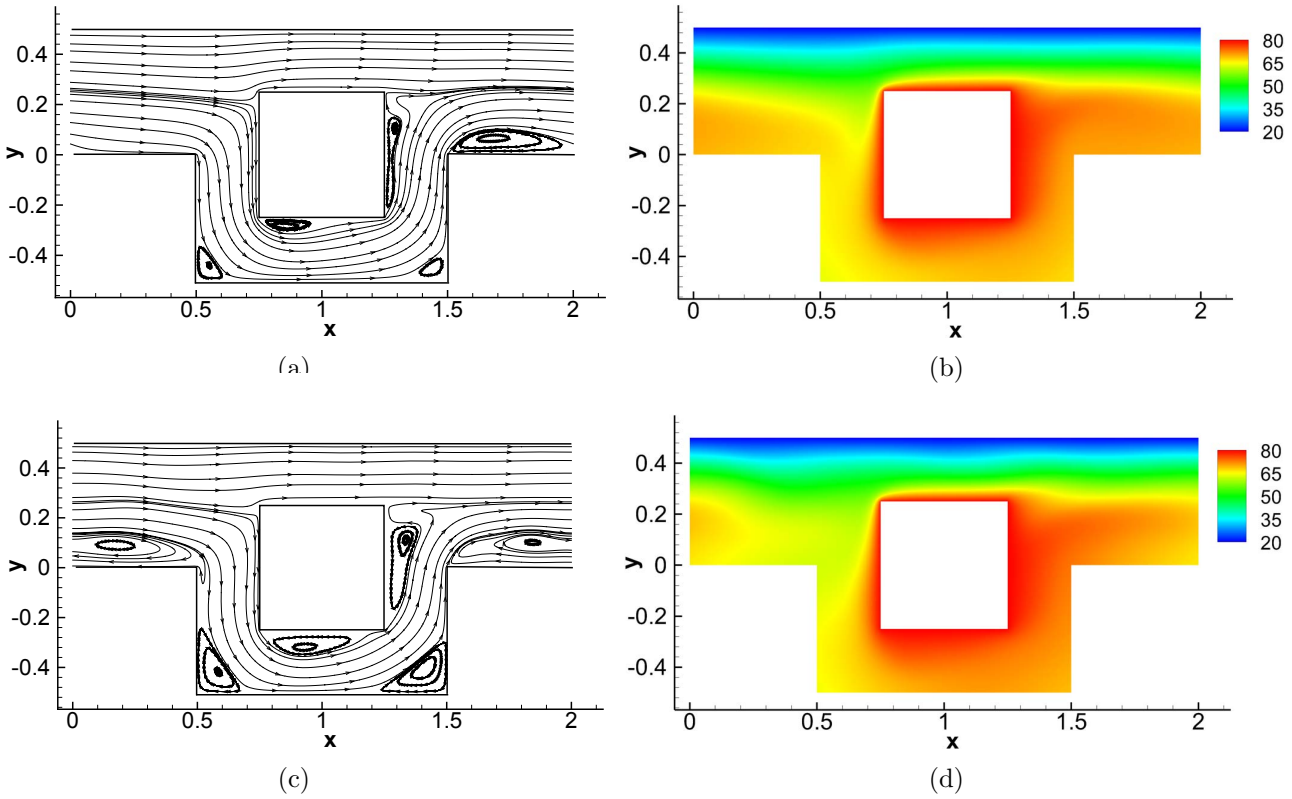

Figure 15 Square cylinder flow: Velocity streamlines and temperature distributions for $Re = 300$ (plots (a) and (b)) and $Re = 1000$ (plots (c) and (d)) with $\alpha = 0.01$

We have computed the time-averaged mean and rms norms of temperature based on the time histories of $T_{L2}(t)$ and $T_{H1}(t)$ to quantitatively demonstrate the overall characteristics of the heat

transfer problem. Table 6 lists the mean and rms values of the temperature obtained with the element order ranging from 3 to 9 for three Reynolds numbers. In these simulations, we employ a time step size $\Delta t = 5e-4$ and $k_0 = 20$ for the lower Reynolds number, i.e., $Re = 300$ and 1000 with thermal diffusivity $\alpha = 0.01$, and $\Delta t = 2e-4$ and $k_0 = 10$ for $Re = 5000$ with $\alpha = 0.001$. The energy constant C_0 is set as $C_0 = 1e3$ for $Re = 300$ and $C_0 = 1e9$ for $Re = 1000$ and 5000. We observe that for $Re = 300$, with element order 4 and above, the computed values for the temperature norms are essentially the same. For $Re = 1000$ and 5000, as the element order increases to 6 and above, the computed values of $T_{L2}(t)$ and $T_{H1}(t)$ become very close. These results suggest that the simulations are numerically converged with respect to the spatial resolution. In the following tests, the values of the element order are employed 6, 7 and 8 for the simulations of $Re = 300$, 1000 and 5000, respectively.

Table 6
Square cylinder flow: Time-averaged mean and rms values of $T_{L2}(t)$ and $T_{H1}(t)$ obtained with various element orders for three Reynolds numbers.

Re	α	Element order	$\overline{T}_{L2}$	T'_{L2}	$\overline{T}_{H1}$	T'_{H1}
300	0.01	3	61.645	0	150.218	0
		4	61.671	0	150.241	0
		5	61.675	0	150.239	0
		6	61.676	0	150.237	0
		7	61.676	0	150.235	0
		8	61.676	0	150.234	0
1000	0.01	3	61.625	1.06e-2	151.206	1.072
		4	61.670	1.02e-2	151.197	1.033
		5	61.681	1.01e-2	151.179	1.013
		6	61.683	1.01e-2	151.194	1.019
		7	61.684	1.01e-2	151.198	1.021
		8	61.684	1.01e-2	151.200	1.023
5000	0.001	3	57.067	9.61e-2	229.036	5.571
		4	56.687	8.26e-2	238.116	5.815
		5	56.742	8.77e-2	238.539	5.711
		6	56.710	8.62e-2	238.676	5.740
		7	56.709	8.43e-2	238.827	5.788
		8	56.710	8.32e-2	238.921	5.812
		9	56.710	8.24e-2	238.990	5.827

The effect of time step size Δt on the accuracy of simulated results has also been studied. Here, we fix the velocity time step size Δt_V and vary the temperature time step size Δt_T. Table 7 lists the mean and rms values of the temperature norms using different Δt_T values for several Reynolds

and Peclet numbers. We employ $C_0 = 1e3, k_0 = 20, \Delta t_V = 5e-4$ for the cases Reynolds number $Re = 300$ with thermal diffusivity $\alpha = 0.01$; $C_0 = 1e9, k_0 = 10, \Delta t_V = 5e-4$ for $Re = 1000$ with $\alpha = 0.001$; $C_0 = 1e9, k_0 = 10, \Delta t_V = 2e-4$ for $Re = 5000$ with $\alpha = 0.001$. As demonstrated in Table 7, the present method can produce stable and accurate results with a large time step size for the $Re = 300$ and 1000. With Δt_T increases, the accuracy of the simulations seems to degrade at a higher or fairly high Reynolds number. This point can also be demonstrated by Fig. 16. The figure shows a comparison of time histories of the temperature norms for $Re = 5000$ with $\alpha = 0.001$. These simulations are performed using an element order 8, $C_0 = 1e9, k_0 = 1, \Delta t_V = 2e-4$. We observe that when Δt_T increase to 0.4, the results seem to lose accuracy for some extent. Note that the simulations using a typical semi-implicit BDF-2 scheme can only produce stable results with $\Delta t_T = 0.002$ or smaller under the same resolution for the case $Re = 5000$ with $\alpha = 0.001$. At this point, the CNAB-2 method can only yield accurate results when Δt_T is less than or equal to 4e-4. However, our method can still maintain an accurate result with $\Delta t_T = 0.02$.

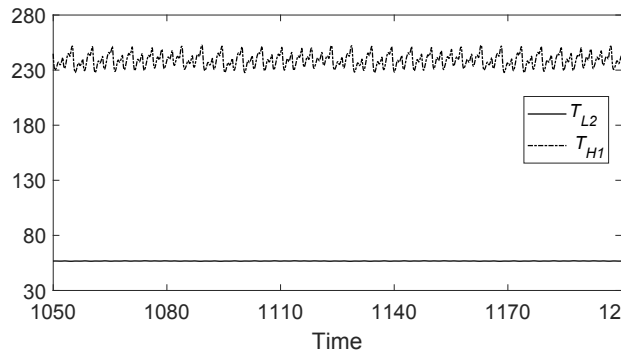

(a) $\Delta t_T = 0.002$

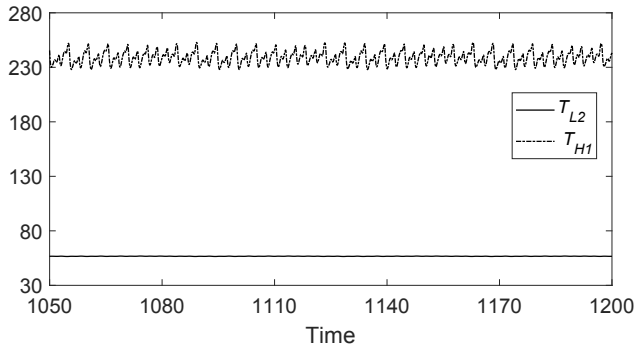

(b) $\Delta t_T = 0.02$

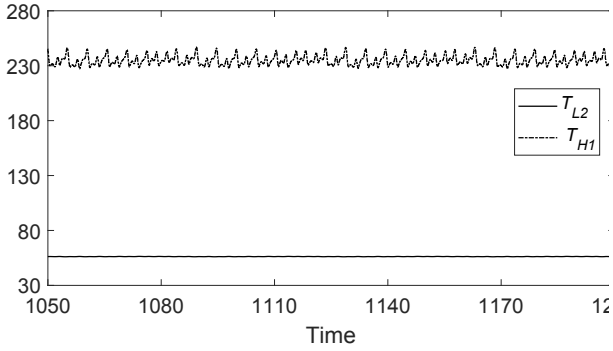

(c) $\Delta t_T = 0.1$

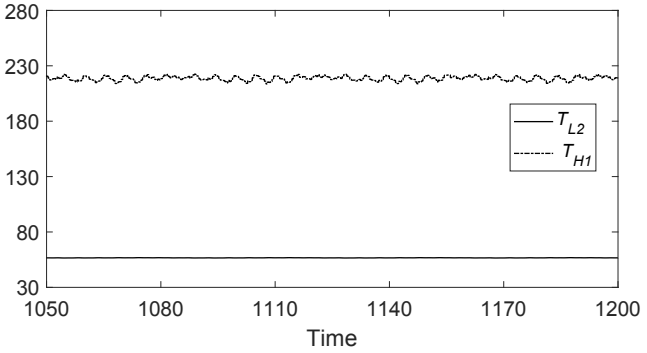

(d) $\Delta t_T = 0.4$

Figure 16 Square cylinder flow: Time histories of the T_{L2} and T_{H1} at $Re = 5000$ with $\alpha = 0.001$, obtained using a range of time step size Δt_T with $k_0 = 1$.

Table 7
Square cylinder flow: Mean and rms values of $T_{L2}(t)$ and $T_{H1}(t)$ at several Reynolds numbers, obtained with a range of temperature time step sizes. The results are computed from the semi-implicit methods and the current method.

Re	Method	Δt_T	$\overline{T}_{L2}$	T'_{L2}	$\overline{T}_{H1}$	T'_{H1}
300	Current	0.0005	61.676	0	150.237	0
		0.025	61.676	0	150.237	0
		0.05	61.676	0	150.237	0
		0.5	61.676	0	150.237	0
		2.5	61.676	0	150.237	0
		5	61.676	0	150.237	0
		25	61.676	0	150.237	0
	Semi-implicit BDF-2	5e-4	61.676	0	150.237	0
		0.0025	61.676	0	150.237	0
		0.0045	**blow up**			
	Semi-implicit CNAB-2	5e-4	61.676	0	150.236	0
		0.001	61.676	0	150.237	0
		0.0025	**blow up**			
1000	Current	5e-4	64.039	3.17e-3	166.724	2.373
		0.005	64.042	3.20e-3	166.751	2.378
		0.05	64.293	2.91e-2	167.162	2.741
		0.25	65.047	1.81e-1	159.508	0.363
		1	64.663	7.64e-2	159.947	0.611
	Semi-implicit BDF-2	5e-4	64.040	3.24e-3	166.716	2.372
		0.001	**blow up**			
	Semi-implicit CNAB-2	5e-4	64.042	3.17e-3	166.704	2.372
		0.001	64.038	3.17e-3	166.726	2.373
		0.0025	**blow up**			
5000	Current	2e-4	56.710	8.32e-2	238.921	5.812
		0.002	56.710	8.32e-2	238.923	5.812
		0.01	56.698	8.32e-2	238.945	5.805
		0.02	56.664	8.31e-2	239.012	5.722
		0.1	58.259	0.150	216.031	**14.087**
	Semi-implicit BDF-2	2e-4	56.710	8.32e-2	238.918	5.812
		0.002	56.724	8.53e-2	239.085	5.738
		0.004	**blow up**			
	Semi-implicit CNAB-2	2e-4	56.707	8.42e-2	239.049	5.834
		4e-4	56.709	8.36e-2	238.959	5.833
		0.001	**blow up**			

We next investigate the effect of the updating frequency Q of the velocity field $\mathbf{u_0}$ on the accuracy of simulations. As $\Delta t_T = N \times \Delta t_V$, the updating frequency Q satisfies that $Q = N \times k_0$. Here, we fix the temperature time step size Δt_T (that is also a fixed N) and update the velocity every k_0 time steps, which is set from 1 to 2000 for Reynolds number Re = 1000 and 5000 with thermal

diffusivity = 0.001. We employ Δt_V= 5e-4 and Δt_T= 0.05 for the simulations corresponding to Re = 1000, and Δt_V= 2e-4 and Δt_T= 0.002 for the cases Re = 5000. The parameter $C_0 = 1e9$ is chosen for all cases. The simulation results are listed in Table 8. For the lower Reynolds number, it can be observed that the accuracy can be guaranteed even at $k_0 = 2000$, while for a higher Reynolds number, the simulation will lose accuracy with a very large k_0. See the cases with Re = 5000, the computed temperature norms are essentially the same when k_0 is no more than 100. However, when k_0 increases to 500, the characteristics of the temperature distribution are notably different. This point can also be demonstrated in Fig. 17, which plots the time histories of T_{L2} and T_{H1} described in Table 8 in the case of $Re = 5000$. These results indicate that, for a high Reynolds number, the velocity field $\mathbf{u_0}$ should be updated more frequently.

Table 8
Square cylinder flow: Mean and rms values of $T_{L2}(t)$ and $T_{H1}(t)$ using a range of k_0 values at Reynolds numbers $Re = 1000$ and 5000. Thermal diffusivity is $\alpha = 0.001$.

Re	k_0	$\overline{T}_{L2}$	T'_{L2}	$\overline{T}_{H1}$	T'_{H1}
1000	1	64.288	8.96e-2	166.689	2.531
	10	64.293	2.91e-2	167.162	2.741
	20	64.290	2.87e-2	167.049	2.674
	50	64.277	2.65e-2	167.087	2.656
	100	64.272	2.60e-2	167.097	2.644
	500	64.274	2.69e-2	167.089	2.639
	1000	64.273	2.66e-2	167.080	2.617
	2000	64.271	2.49e-2	167.073	2.602
5000	1	56.710	8.32e-2	238.923	5.812
	10	56.710	8.32e-2	238.923	5.812
	20	56.710	8.32e-2	238.923	5.812
	50	56.710	8.32e-2	238.922	5.811
	100	56.710	8.32e-2	238.921	5.811
	500	56.629	10.023	503.524	**7935.640**
	2000	56.915	8.53e-2	224.007	**7.353**

Finally, Fig. 18 illustrates the dynamic of the square cylinder flow with a temporal sequence of snapshots of the velocity field at the Reynolds number $Re = 5000$. Fig. 19 shows the temporal sequence of snapshots of temperature fields at thermal diffusivity $\alpha = 0.001$ corresponding to the velocity field. Here we have employed element order 8, $C_0 = 1e9$ and $k_0 = 1$. A time step size $\Delta t = 2e - 4$ is used for the solution of both temperature and velocity field. A continuous vortices moving can be observed. These vortices generate near the walls and flow past the right side. Besides, a prominent feature of this flow lies in that the re-entering vortices interact with the

square cylinder due to the periodicity. Such interactions give rise to some vortices hitting on the left wall of the cylinder and then split into two ways and new vortices near the wall are spawn. Such a complex flow pattern makes a complicated temperature distribution in the T-shape channel.

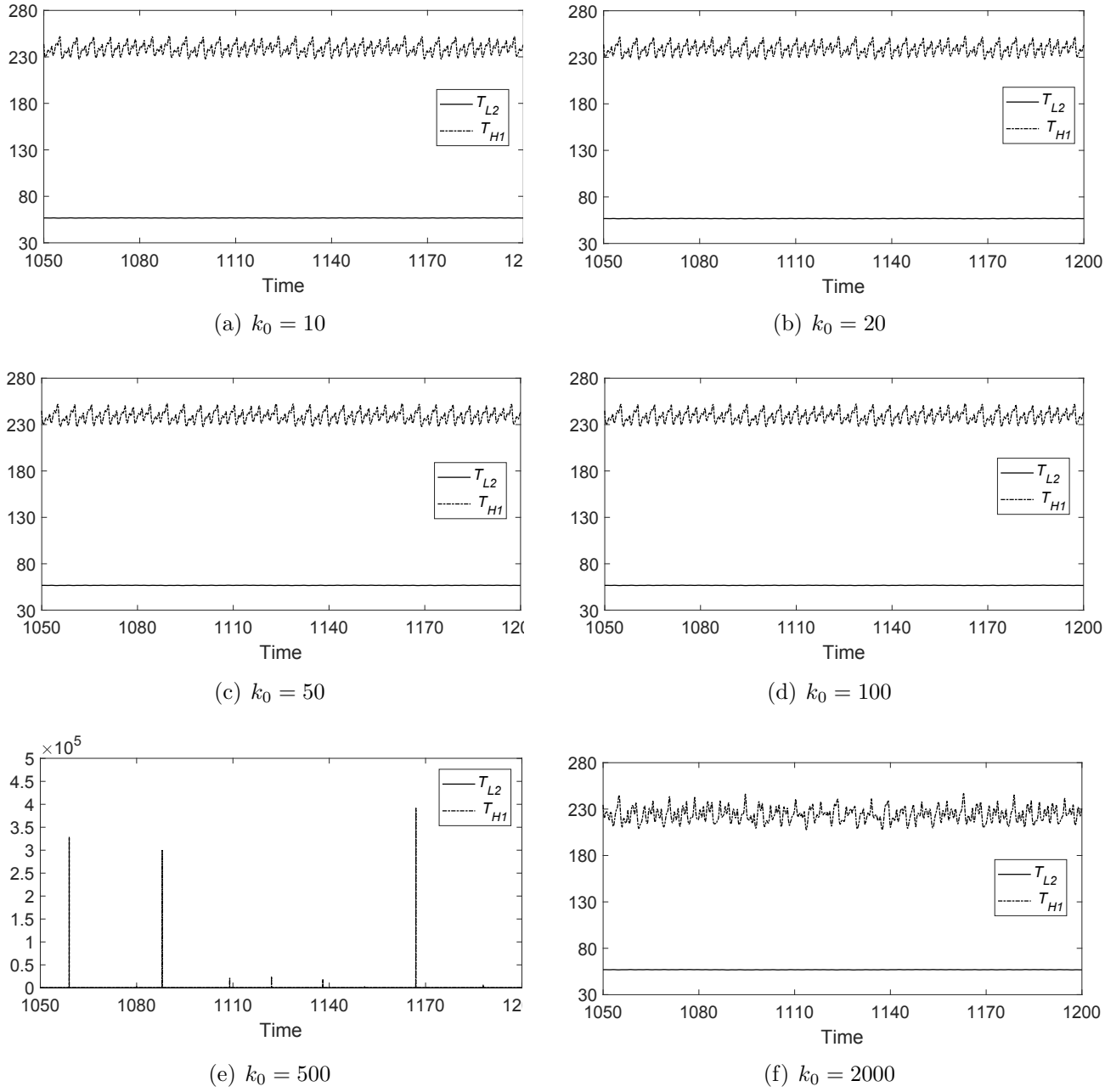

(a) $k_0 = 10$ (b) $k_0 = 20$

(c) $k_0 = 50$ (d) $k_0 = 100$

(e) $k_0 = 500$ (f) $k_0 = 2000$

Figure 17 Square cylinder flow: Time histories of the T_{L2} and T_{H1} at Reynolds number $Re = 5000$ with $\alpha = 0.001$ and time step size $\Delta t_T = 0.002$, obtained using a range of k_0 values.

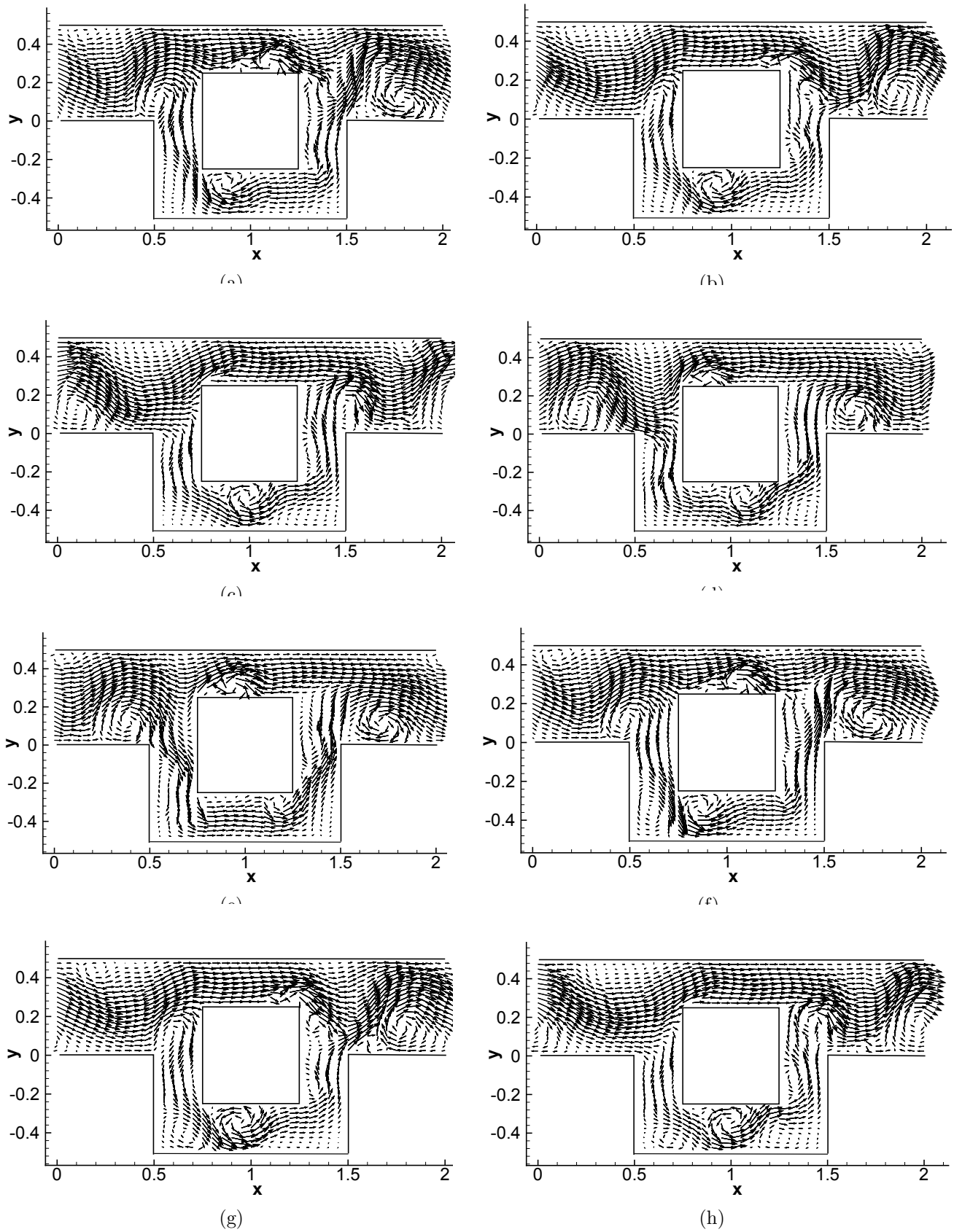

Figure 18 Square cylinder flow: Temporal sequence of snapshots of the velocity fields at Reynolds number $Re = 5000$, (a) $t = t_0$, (b)$t = t_0 + 5$, (c) $t = t_0 + 10$, (d)$t = t_0 + 15$, (e) $t = t_0 + 20$, (f) $t = t_0 + 25$, (g) $t = t_0 + 30$, (h) $t = t_0 + 35$. t_0 denotes the initial time instance of the sequence.

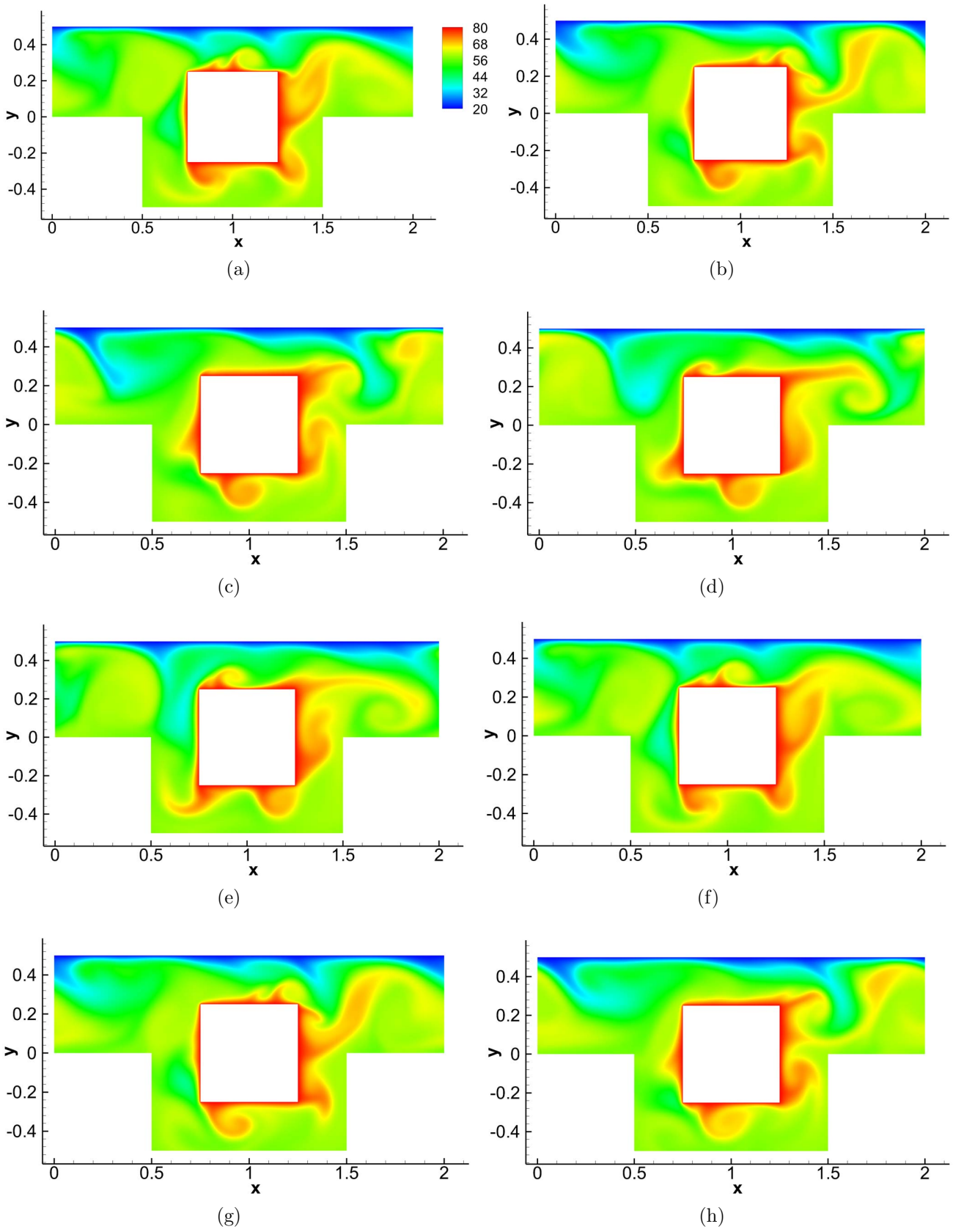

Figure 19 Square cylinder flow: Temporal sequence of snapshots of the temperature fields at Reynolds number $Re = 5000$ and thermal diffusivity $\alpha = 0.001$, at identical time instance as in Fig. 18, (a) $t = t_0$, (b)$t = t_0 + 5$, (c) $t = t_0 + 10$, (d)$t = t_0 + 15$, (e) $t = t_0 + 20$, (f) $t = t_0 + 25$, (g) $t = t_0 + 30$, (h) $t = t_0 + 35$.

4. Concluding remarks

In the current work we have presented an unconditionally energy stable scheme for convective heat transfer simulations. The scheme endows a discrete energy stability property, and stable results can be obtained irrespective of the time step size. The developed scheme also features an expanded accuracy range compared with the common-used semi-implicit scheme. It is observed that our algorithm can provide accurate simulation results at a large or fairly large time step size. The salient property of the scheme lies in the gPAV-based reformulation and the numerical treatment of the convection term. In the reformulated system, the convection term is replaced by a linear term and a correction term, and the correction term is placed under the control of an auxiliary variable. Within each time step, the energy stable scheme requires the computation of two temperature fields by solving the temperature linear algebraic system involving a coefficient matrix updated periodically. The auxiliary variable is given by a well-defined explicit formulation, which guarantees the positivity of its computational value.

Extensive numerical experiments have been provided with several convective heat transfer problems in fluid flows. The numerical tests demonstrated the unconditional energy stability of the proposed scheme. Besides, at a large or fairly large time step size, accurate simulation results can also be achieved by our method. The update frequency k_0 of velocity $\mathbf{u_0}$ has an impact on the accuracy range of the simulation results for the high or fairly high Reynolds number fluid flow. Normally, for a relatively low Reynolds number, the k_0 has a very small effect on the accuracy of the results, thus one can select a high (such as 1000 for $R_e = 1000$ in the circular cylinder flow case); while for a high Reynolds number, the velocity field should be updated more frequently. Overall, with an overly large k_0, the simulation will lose the accuracy at a large time step size. The results show that the allowed maximum time step size that can achieve accurate simulation results with our scheme is typically considerably larger than that with the semi-implicit type scheme or the modied scheme from Remark 2.3. We anticipate that combing with the unconditional energy-stable scheme for incompressible Navier-Stokes equations, the presented scheme can be a powerful tool for efficient simulations of convective heat transfer problems and beyond.

Appendix A Numerical algorithm for incompressible Navier-Stokes equations

We adopt the semi-implicit scheme herein to solve the incompressible Navier-Stokes Eqs. (1a) - (1b) together with the boundary condition (4) and the initial condition (8). A summary of the

numerical algorithm is presented in this appendix.

The same notation is utilized here as in the main text.

Given $\mathbf{u}^n$ we compute p^{n+1} and $\mathbf{u}^{n+1}$ successively in a de-coupled fashion as follows:

For p^{n+1}:

$$\frac{\gamma_0\tilde{\mathbf{u}}^{n+1}-\hat{\mathbf{u}}}{\Delta t}+\mathbf{u}^{*,n+1}\cdot\nabla\mathbf{u}^{*,n+1}+\nabla p^{n+1}+\nu\nabla\times\nabla\times\mathbf{u}^{*,n+1}=\mathbf{f}^{n+1}, \tag{42a}$$

$$\nabla\cdot\tilde{\mathbf{u}}^{n+1}=0, \tag{42b}$$

$$\mathbf{n}\cdot\tilde{\mathbf{u}}^{n+1}=\mathbf{n}\cdot\mathbf{w}^{n+1}, \quad \text{on } \partial\Omega. \tag{42c}$$

For $\mathbf{u}^{n+1}$:

$$\frac{\gamma_0\mathbf{u}^{n+1}-\gamma_0\tilde{\mathbf{u}}^{n+1}}{\Delta t}-\nu\nabla^2\mathbf{u}^{n+1}=\nu\nabla\times\nabla\times\mathbf{u}^{*,n+1}, \tag{43a}$$

$$\mathbf{u}^{n+1}=\mathbf{w}^{n+1}, \quad \text{on } \partial\Omega. \tag{43b}$$

In the above equations, $\tilde{\mathbf{u}}^{n+1}$ is an auxiliary variable approximating $\mathbf{u}^{n+1}$ and J ($J=1$ or 2) denotes the temporal order of accuracy as in main text. γ_0 is defined by:

$$\gamma_0=\begin{cases}1, & J=1,\\ 3/2, & J=2,\end{cases} \tag{44}$$

and $\hat{\mathbf{u}}$ and $\mathbf{u}^{*,n+1}$ are defined by

$$\hat{\mathbf{u}}=\begin{cases}\mathbf{u}^n, & J=1,\\ 2\mathbf{u}^n-\frac{1}{2}\mathbf{u}^{n-1}, & J=2;\end{cases} \quad \mathbf{u}^{*,n+1}=\begin{cases}\mathbf{u}^n, & J=1,\\ 2\mathbf{u}^n-\mathbf{u}^{n-1}, & J=2.\end{cases} \tag{45}$$

The weak form for the pressure p^{n+1} can be derived from Eqs. (42a)-(42c), which is given by,

$$\int_\Omega\nabla p^{n+1}\cdot\nabla q=\int_\Omega\mathbf{G}^{n+1}\cdot\nabla q-\nu\int_{\partial\Omega}\mathbf{n}\times\omega^{*,n+1}\cdot\nabla q-\frac{\gamma_0}{\Delta t}\int_{\partial\Omega}\mathbf{n}\cdot\mathbf{w}^{n+1}q, \quad \forall q\in H^1(\Omega), \tag{46}$$

where $\mathbf{G}^{n+1}=\mathbf{f}^{n+1}+\frac{\hat{\mathbf{u}}}{\Delta t}-\mathbf{u}^{*,n+1}\cdot\nabla\mathbf{u}^{*,n+1}$ and $\omega=\nabla\times\mathbf{u}$. For the velocity, the weak form is given

by,

$$\frac{\gamma_0}{\nu\Delta t}\int_\Omega \mathbf{u}^{n+1}\varphi + \int_\Omega \nabla\varphi\cdot\nabla\mathbf{u}^{n+1} = \frac{1}{\nu}\int_\Omega \left(\mathbf{G}^{n+1}-\nabla p^{n+1}\right)\varphi, \quad \forall\varphi\in H^1(\Omega) \text{ with } \varphi|_{\partial\Omega_d}=0. \quad (47)$$

The weak forms in (46) and (47) can be discretized using C^0 spectral elements in the standard fashion. Within each time step, we first solve Eq. (46) for p^{n+1} and then solve Eq. (47), together with the boundary condition (4), for $\mathbf{u}^{n+1}$. It is worth noting that the auxiliary variable $\tilde{\mathbf{u}}^{n+1}$ is not explicitly computed.

Appendix B Semi-implicit algorithms for solving the convective heat transfer equation

A summary of the semi-implicit algorithms to solve the convective heat transfer equation (1c) combined with the boundary condition (6)-(7) and initial condition (9) are presented in this subsection. The two employed semi-implicit methods are second-order backward differentiation formula (BDF-2) and Crank-Nicolson Adam-Bashforth (CNAB-2) methods.

Semi-implicit BDF-2 algorithm for solving the convective heat transfer equation

Here, we utilize the same notation as in the main text. Given T^n and $\mathbf{u^{n+1}}$, we can compute T^{n+1} based on the BDF-2 scheme (Liu et al. (2020); Qaddah et al. (2022)), which reads as follows:

$$\frac{\gamma_0 T^{n+1}-\hat{T}}{\Delta t} + \mathbf{u}^{n+1}\cdot\nabla T^{*,n+1} = \alpha\nabla^2 T^{n+1} + g^{n+1}(\mathbf{x},t), \quad (48a)$$

$$T^{n+1} = T_d^{n+1}(\mathbf{x},t), \quad \text{on } \partial\Omega_d, \quad (48b)$$

$$\mathbf{n}\cdot\nabla T^{n+1} = g_c^{n+1}(\mathbf{x},t), \quad \text{on } \partial\Omega_n. \quad (48c)$$

In the above equations, the detailed definition of all the related variables can be found in Section 2.3. Furthermore, we can employ the C^0-continuous high-order spectral elements for spatial

discretizations. The weak form about T^{n+1} is given as follows,

$$\begin{aligned}&\int_\Omega \nabla T^{n+1}\cdot\nabla\varphi d\Omega+\frac{\gamma_0}{\alpha\Delta t}\int_\Omega T^{n+1}\varphi d\Omega\\&=\frac{1}{\alpha}\int_\Omega\left(g^{n+1}+\frac{\hat{T}}{\Delta t}-\mathbf{u}^{n+1}\cdot\nabla T^{*,n+1}\right)\varphi d\Omega+\int_{\partial\Omega_n}g_c^{n+1}\varphi dA,\quad\forall\varphi\text{ with }\ \varphi|_{\partial\Omega_d}=0.\end{aligned}\tag{49}$$

where we have used integration by parts, the divergence theorem, and the equation (50c).

Semi-implicit CNAB-2 algorithm for solving the convective heat transfer equation

Given T^n and $\mathbf{u^{n+1}}$, we can compute T^{n+1} based on the following CN-AB scheme:

$$\frac{T^{n+1}-T^n}{\Delta t}+\mathbf{u}^{n+\frac{1}{2}}\cdot\nabla T^{*,n+\frac{1}{2}}=\alpha\nabla^2T^{n+\frac{1}{2}}+g^{n+\frac{1}{2}}(\mathbf{x},t),\tag{50a}$$

$$T^{n+1}=T_d^{n+1}(\mathbf{x},t),\quad\text{ on }\partial\Omega_d,\tag{50b}$$

$$\mathbf{n}\cdot\nabla T^{n+1}=g_c^{n+1}(\mathbf{x},t),\quad\text{ on }\partial\Omega_n,\tag{50c}$$

where

$$\mathbf{u}^{n+\frac{1}{2}}=\frac{1}{2}(\mathbf{u}^{n+1}+\mathbf{u}^n),\quad T^{n+\frac{1}{2}}=\frac{1}{2}(T^{n+1}+T^n),\quad g^{n+\frac{1}{2}}=\frac{1}{2}(g^{n+1}+g^n),\tag{51}$$

and

$$T^{*,n+\frac{1}{2}}=\frac{3}{2}T^n-\frac{1}{2}T^{n-1}.\tag{52}$$

Furthermore, we can employ the C^0-continuous high-order spectral elements for spatial discretizations. The weak form about T^{n+1} is given as follows,

$$\begin{aligned}&\int_\Omega\nabla T^{n+1}\cdot\nabla\varphi d\Omega+\frac{2}{\alpha\Delta t}\int_\Omega T^{n+1}\varphi d\Omega\\&=\frac{2}{\alpha}\int_\Omega\left(g^{n+\frac{1}{2}}+\frac{T^n}{\Delta t}-\mathbf{u}^{n+\frac{1}{2}}\cdot\nabla T^{*,n+\frac{1}{2}}\right)\varphi d\Omega+\int_{\partial\Omega_n}g_c^{n+1}\varphi dA\\&+\int_{\partial\Omega}\mathbf{u}\cdot\nabla T^n\varphi dA-\int_\Omega\nabla T^n\cdot\nabla\varphi d\Omega,\quad\forall\varphi\text{ with }\ \varphi|_{\partial\Omega_d}=0,\end{aligned}\tag{53}$$

where we have used integration by parts, the divergence theorem, and the equation (50c).

Appendix C A more detailed derivation of equations (15) and (18)

In this appendix, we derive the governing equations of the gPAV style reformulated system, which corresponds to equaitons (15) and (18). As pointed out in Section 2.2, the reformulated system is the core and key to develope the discretely energy-stable scheme. In light of $\frac{R^2(t)}{E(t)} = 1$ on the continuum level, the reformulation is realized by incorporating a number of identically zero terms into the original equations.

Derivation of Equations (15)

With $\frac{R^2(t)}{E(t)} = 1$ on the continuum level, the convective heat transfer equation (1c) can be written as,

$$\frac{\partial T}{\partial t} + \frac{R^2(t)}{E(t)} N(\mathbf{u}, T) = \alpha \nabla^2 T + [\frac{R^2(t)}{E(t)} - 1] M(\mathbf{u_0}, T) + g(\mathbf{x}, t). \tag{54}$$

Note that the $M(\mathbf{u_0}, T)$ is a linear approximation of $N(\mathbf{u}, T)$. By moving the terms associated with $\frac{R^2(t)}{E(t)}$ to the right hand, the equation (54) can be further transformed into equations (15), which is an equivalent form of equations (1c) at the continuum level.

Derivation of Equations (18)

With $\frac{R^2(t)}{E(t)} = 1$, we incorporate three zero terms into the right hand side (RHS) of Eq. (14),

$$\begin{aligned} 2R\frac{dR}{dt} = & \int_\Omega T \cdot \frac{\partial T}{\partial t} d\Omega \\ & + \left[\frac{R^2(t)}{E(t)} - 1\right] \int_\Omega \left[-M(\mathbf{u_0}, T) + \alpha \nabla^2 T + g(\mathbf{x}, t)\right] T d\Omega \\ & + \frac{R^2(t)}{E(t)} \left(\int_\Omega \left[M(\mathbf{u_0}, T) - N(\mathbf{u}, T)\right] T d\Omega - \int_\Omega \left[M(\mathbf{u_0}, T) - N(\mathbf{u}, T)\right] T d\Omega \right) \\ & + \left[1 - \frac{R^2(t)}{E(t)}\right] \left(\left| \int_\Omega g(\mathbf{x}, t) T d\Omega \right| + \left| \int_{\partial\Omega} \left[\alpha \mathbf{n} \cdot \nabla T - \frac{1}{2}(\mathbf{n} \cdot \mathbf{u}) T\right] T dA \right| \right). \end{aligned} \tag{55}$$

Such reformulation follows the gPAV idea presented in Yang & Dong (2020). The equation that includes three identically zero terms presents an equivalent form of equations (14) at the continuum level.

The equation (55) can be further transformed into

$$
\begin{aligned}
2R\frac{dR}{dt} &= \int_\Omega T\cdot\frac{\partial T}{\partial t}d\Omega \\
&\quad + \frac{R^2(t)}{E(t)}\int_\Omega \left[-M(\mathbf{u_0},T)+\alpha\nabla^2 T+g(\mathbf{x},t)\right]Td\Omega \\
&\quad + \frac{R^2(t)}{E(t)}\int_\Omega \left[M(\mathbf{u_0},T)-N(\mathbf{u},T)\right]Td\Omega \\
&\quad - \int_\Omega \left[-M(\mathbf{u_0},T)+\alpha\nabla^2 T+g(\mathbf{x},t)\right]Td\Omega \\
&\quad - \frac{R^2(t)}{E(t)}\int_\Omega \left[M(\mathbf{u_0},T)-N(\mathbf{u},T)\right]Td\Omega \\
&\quad + \left[1-\frac{R^2(t)}{E(t)}\right]\left(\left|\int_\Omega g(\mathbf{x},t)Td\Omega\right| + \left|\int_{\partial\Omega}\left[\alpha\mathbf{n}\cdot\nabla T-\frac{1}{2}(\mathbf{n}\cdot\mathbf{u})T\right]TdA\right|\right) \\
&= \int_\Omega T\cdot\frac{\partial T}{\partial t}d\Omega + \frac{R^2(t)}{E(t)}\int_\Omega \left[-N(\mathbf{u},T)+\alpha\nabla^2 T+g(\mathbf{x},t)\right]Td\Omega \\
&\quad - \int_\Omega \left[-M(\mathbf{u_0},T)+\alpha\nabla^2 T+g(\mathbf{x},t)+\frac{R^2(t)}{E(t)}\left(M(\mathbf{u_0},T)-N(\mathbf{u},T)\right)\right]Td\Omega \\
&\quad + \left[1-\frac{R^2(t)}{E(t)}\right]\left(\left|\int_\Omega g(\mathbf{x},t)Td\Omega\right| + \left|\int_{\partial\Omega_d}\left[\alpha\mathbf{n}\cdot\nabla T-\frac{1}{2}(\mathbf{n}\cdot\mathbf{u})T_d\right]T_d dA\right.\right. \\
&\quad \left.\left. + \int_{\partial\Omega_n}\left[\alpha g_c(\mathbf{x},t)-\frac{1}{2}(\mathbf{n}\cdot\mathbf{u})T\right]TdA\right|\right),
\end{aligned}
\tag{56}
$$

where $\partial\Omega=\partial\Omega_d\cup\partial\Omega_n$. In light of the energy balance equation (11), we obtain that

$$
\begin{aligned}
&\int_\Omega \left[-N(\mathbf{u},T)+\alpha\nabla^2 T+g(\mathbf{x},t)\right]Td\Omega = -\alpha\int_\Omega |\nabla T|^2 d\Omega + \int_\Omega g(\mathbf{x},t)Td\Omega \\
&+\int_{\partial\Omega_d}\left[\alpha\mathbf{n}\cdot\nabla T-\frac{1}{2}(\mathbf{n}\cdot\mathbf{u})T_d\right]T_d dA + \int_{\partial\Omega_n}\left[\alpha g_c(\mathbf{x},t)-\frac{1}{2}(\mathbf{n}\cdot\mathbf{u})T\right]TdA.
\end{aligned}
\tag{57}
$$

Then we finally attain the equation (18) as follows,

$$
\begin{aligned}
2R\frac{dR}{dt} &= \int_{\Omega} T \cdot \frac{\partial T}{\partial t} d\Omega \\
&+ \frac{R^2(t)}{E(t)} \left[-\alpha \int_{\Omega} |\nabla T|^2 d\Omega + \int_{\Omega} g(\mathbf{x}, t) T d\Omega \right. \\
&+ \int_{\partial\Omega_d} \left[\alpha \mathbf{n} \cdot \nabla T - \frac{1}{2}(\mathbf{n} \cdot \mathbf{u}) T_d \right] T_d dA + \left. \int_{\partial\Omega_n} \left[\alpha g_c(\mathbf{x}, t) - \frac{1}{2}(\mathbf{n} \cdot \mathbf{u}) T \right] T dA \right] \\
&- \int_{\Omega} \left[-M(\mathbf{u_0}, T) + \alpha \nabla^2 T + g(\mathbf{x}, t) + \frac{R^2(t)}{E(t)} (M(\mathbf{u_0}, T) - N(\mathbf{u}, T)) \right] T d\Omega \\
&+ \left[1 - \frac{R^2(t)}{E(t)} \right] \left(\left| \int_{\Omega} g(\mathbf{x}, t) T d\Omega \right| + \left| \int_{\partial\Omega_d} \left[\alpha \mathbf{n} \cdot \nabla T - \frac{1}{2}(\mathbf{n} \cdot \mathbf{u}) T_d \right] T_d dA \right. \right. \\
&+ \left. \left. \int_{\partial\Omega_n} \left[\alpha g_c(\mathbf{x}, t) - \frac{1}{2}(\mathbf{n} \cdot \mathbf{u}) T \right] T dA \right| \right).
\end{aligned}
\tag{58}
$$

References

Bharti, R. P., Chhabra, R. P., & Eswaran, V. (2007). A numerical study of the steady forced convection heat transfer from an unconfined circular cylinder. *Heat and Mass Transfer*, *43*, 639–648.

Bhinder, A. P. S., Sarkar, S., & Dalal, A. (2012). Flow over and forced convection heat transfer around a semi-circular cylinder at incidence. *International Journal of Heat and Mass Transfer*, *55*, 5171–5184.

Blackburn, H. M., & Henderson, R. D. (1999). A study of two-dimensional flow past an oscillating cylinder. *Journal of Fluid Mechanics*, *385*, 255–286.

Bo, T., Iacovides, H., & Launder, B. (1995). Convective discretization schemes for the turbulence transport equations in flow predictions through sharp u-bends. *International Journal of Numerical Methods for Heat and Fluid Flow*, *5*, 33–48.

Celledoni, E., Grimm, V., Mclachlan, R. I., Mclaren, D. I., ONeale, D., Owren, B., & Quispel, G. R. W. (2012). Preserving energy resp. dissipation in numerical PDEs using the "Average Vector Field" method. *Journal of Computational Physics*, *231*.

Chandra, A., & Chhabra, R. (2011). Flow over and forced convection heat transfer in Newtonian fluids from a semi-circular cylinder. *International Journal of Heat and Mass Transfer*, *54*, 225–241.

Chen, C., & Yang, X. (2019). Efficient numerical scheme for a dendritic solidification phase field model with melt convection. *Journal of Computational Physics*, *388*, 41–62.

Chen, H., Sun, S., & Zhang, T. (2018). Energy stability analysis of some fully discrete numerical schemes for incompressible Navier–Stokes equations on staggered grids. *Journal of Scientific Computing*, *75*, 427–456.

Cheng, Q., & Shen, J. (2018). Multiple scalar auxiliary variable (MSAV) approach and its application to the phase-field vesicle membrane model. *SIAM Journal on Scientific Computing*, *40*, A3982–A4006.

Dahlby, M., & Owren, B. (2011). A general framework for deriving integral preserving numerical methods for pdes. *SIAM Journal on Scientific Computing*, *33*, 2318–2340.

Eidnes, S., Owren, B., & Ringholm, T. (2018). Adaptive energy preserving methods for partial differential equations. *Advances in Computational Mathematics*, *44*, 815–839.

Feldman, Y. (2018). Semi-implicit direct forcing immersed boundary method for incompressible viscous thermal flow problems: A Schur complement approach. *International Journal of Heat and Mass Transfer*, *127*, 1267–1283.

Gong, Y., Zhao, J., Yang, X., & Wang, Q. (2018). Fully discrete second-order linear schemes for hydrodynamic phase field models of binary viscous fluid flows with variable densities. *SIAM Journal on Scientific Computing*, *40*, B138–B167.

Jiang, N., Mohebujjaman, M., Rebholz, L. G., & Trenchea, C. (2016). An optimally accurate discrete regularization for second order timestepping methods for navier–stokes equations. *Computer Methods in Applied Mechanics and Engineering*, *310*, 388–405.

Karniadakis, G. E., & Sherwin, S. J. (2005). *Spectral/HP Element Methods for Computational Fluid Dynamics*. (2nd ed.). Oxford University Press,.

Labovsky, A., Layton, W. J., Manica, C. C., Neda, M., & Rebholz, L. G. (2009). The stabilized extrapolated trapezoidal finite-element method for the Navier–Stokes equations. *Computer Methods in Applied Mechanics and Engineering*, *198*, 958–974.

Li, J., Zhao, J., & Wang, Q. (2019). Energy and entropy preserving numerical approximations of thermodynamically consistent crystal growth models. *Journal of Computational Physics*, *382*, 202–220.

Lin, L., Liu, X., & Dong, S. (2020a). A gPAV-based unconditionally energy-stable scheme for incompressible flows with outflow/open boundaries. *Computer Methods in Applied Mechanics and Engineering*, *365*, 112969.

Lin, L., Ni, N., Yang, Z., & Dong, S. (2020b). An energy-stable scheme for incompressible Navier-Stokes equations with periodically updated coefficient matrix. *Journal of Computational Physics*, *418*, 109624.

Lin, L., Yang, Z., & Dong, S. (2019). Numerical approximation of incompressible navier-stokes equations based on an auxiliary energy variable. *Journal of Computational Physics*, *388*, 1–22.

Liu, X., Xie, Z., & Dong, S. (2020). On a simple and effective thermal open boundary condition for convective heat transfer problems. *International Journal of Heat and Mass Transfer*, *151*, 119355.

Pan, J., Su, H., & Feng, X. (2021). Effective velocity-correction projection methods for unsteady incompressible natural convection equations. *International Communications in Heat and Mass Transfer*, *121*, 104860.

Qaddah, B., Soucasse, L., Doumenc, F., Mergui, S., Rivire, P., & Soufiani, A. (2022). Influence of turbulent natural convection on heat transfer in shallow caves. *International Journal of Thermal Sciences*, *177*, 107524.

Qian, Y., Yang, Z., Wang, F., & Dong, S. (2020). gPAV-based unconditionally energy-stable schemes for the Cahn-Hilliard equation: Stability and error analysis. *Computer Methods in Applied Mechanics and Engineering*, *372*, 113444.

Rakotondrandisa, A., Sadaka, G., & Danaila, I. (2020). A finite-element toolbox for the simulation of solid-iquid phase-change systems with natural convection. *Computer Physics Communications*, *253*, 107188.

Sanderse, B. (2013). Energy-conserving Runge–Kutta methods for the incompressible Navier-Stokes equations. *Journal of Computational Physics*, *233*, 100–131.

Seo, Y. M., Luo, K., Ha, M. Y., & Park, Y. G. (2020). Direct numerical simulation and artificial neural network modeling of heat transfer characteristics on natural convection with a sinusoidal cylinder in a long rectangular enclosure. *International Journal of Heat and Mass Transfer*, *152*, 119564.

Shen, J., Xu, J., & Yang, J. (2018). The scalar auxiliary variable (SAV) approach for gradient flows. *Journal of Computational Physics*, *353*, 407–416.

Sherwin, S., & Karniadakis, G. E. (1995). A triangular spectral element method; applications to the incompressible navier-stokes equations. *Computer methods in applied mechanics and engineering*, *123*, 189–229.

Simo, J., & Armero, F. (1994). Unconditional stability and long-term behavior of transient algorithms for the incompressible Navier-Stokes and Euler equations. *Computer Methods in Applied Mechanics and Engineering*, *111*, 111–154.

Son, J. H., & Park, I. S. (2021). Numerical investigation of electro-thermo-convection and heat transfer enhancement in a square enclosure with various electrode arrangements. *Case Studies in Thermal Engineering*, *28*, 101650.

Soo, M., Riaz, Amir, Aute, & Vikrant (2017). Direct numerical simulation of incompressible multiphase flow with phase change. *Journal of Computational Physics*, *344*, 381–418.

Verstappen, R., & Veldman, A. (2003). Symmetry-preserving discretization of turbulent flow. *Journal of Computational Physics*, *187*, 343–368.

Wang, X., & Pepper, D. W. (2009). Numerical simulation for natural convection in vertical channels. *International Journal of Heat and Mass Transfer*, *52*, 4095–4102.

Woodruff, C. (2022). An efficient and accurate numerical scheme for long time statistical properties of the infinite Prandtl number model for convection. *Journal of Mathematical Analysis and Applications*, *509*, 125944.

Yan, H., Luo, L., Zhang, J., Du, W., Huang, D., & Wang, S. (2022). Numerical analysis of heat transfer characteristics in a pin fin-dimpled channel with different pin fins and dimple locations. *International Journal of Numerical Methods for Heat & Fluid Flow*, *32*, 3132–3158.

Yang, X. (2016). Linear, first and second-order, unconditionally energy stable numerical schemes for the phase field model of homopolymer blends. *Journal of Computational Physics*, *327*, 294–316.

Yang, Z., & Dong, S. (2019). An unconditionally energy-stable scheme based on an implicit auxiliary energy variable for incompressible two-phase flows with different densities involving only precomputable coefficient matrices. *Journal of Computational Physics*, *393*, 229–257.

Yang, Z., & Dong, S. (2020). A roadmap for discretely energy-stable schemes for dissipative systems based on a generalized auxiliary variable with guaranteed positivity. *Journal of Computational Physics*, *404*, 109121.

Yang, Z., Lin, L., & Dong, S. (2019). A family of second-order energy-stable schemes for Cahn-Hilliard type equations. *Journal of Computational Physics*, *383*, 24–54.

Yoon, H. S., Nam, S. H., & Kim, M. I. (2020). Effect of the geometric features of the harbor seal vibrissa based biomimetic cylinder on the forced convection heat transfer. *International Journal of Heat and Mass Transfer*, *159*, 120086.

Zhang, J., & Yang, X. (2020). A fully decoupled, linear and unconditionally energy stable numerical scheme for a melt-convective phase-field dendritic solidification model. *Computer Methods in Applied Mechanics and Engineering*, *363*, 112779.

Zhang, N., Zheng, Z., & Eckels, S. (2008). Study of heat-transfer on the surface of a circular cylinder in flow using an immersed-boundary method. *International Journal of Heat and Fluid Flow*, *29*, 1558–1566.

Zhao, J., Yang, X., Gong, Y., Zhao, X., Yang, X., Li, J., & Wang, Q. (2018). A general strategy for numerical approximations of non-equilibrium models–part i thermodynamical systems. *Int. J. Numer. Anal. Model.*, *15*, 884–918.

Zheng, X., Babaee, H., Dong, S., Chryssostomidis, C., & Karniadakis, G. E. (2015). A phase-field method for 3d simulation of two-phase heat transfer. *International Journal of Heat and Mass Transfer*, *82*, 282–298.

Zheng, X., & Dong, S. (2011). An eigen-based high-order expansion basis for structured spectral elements. *Journal of Computational Physics*, *230*, 8573–8602.